ETHZ-IPP Internal Report 2006-01
März 2006

Helicity analysis of ρ^0 mesons from diffractive photoproduction at HERA

DIPLOMA THESIS

presented by
Erik Magnus Bodin

Prof. Dr. Ralph A. Eichler, Supervisor

Dr. Benno List, Advisor

Institute for Particle Physics
ETH Zurich, Switzerland

April 4, 2006

Abstract

The helicity properties of diffractively photoproduced ρ mesons have been investigated. Especially the spin density matrix elements r^{04}_{00}, Re$[r^{04}_{10}]$ and r^{04}_{1-1} that contain information of how the helicities of the photon and the vector meson are correlated were studied. The matrix elements were determined as functions of the kinematic variables W, the invariant mass of the proton-photon system, and t, the transfered four momentum, in the range $25 < W < 65$ GeV and $|t| > 0$ GeV^2. The analysis was based on data from the H1 detector from 2005 with an integrated luminosity of 570 nb^{-1}. The spin density matrix elements were extracted by fitting the angular distribution for the decay $\rho \to \pi^+ + \pi^-$ to a theoretical model. The analysis shows a strong t-dependence of the matrix elements r^{04}_{00} and r^{04}_{1-1}, both being consistent with zero in the low-t region $|t| < 1.0$ GeV^2 and non-zero in the high t-region. For $|t| > 1.0$ GeV^2, r^{04}_{00} is positive whereas r^{04}_{1-1} is negative. Re$[r^{04}_{10}]$ is consistent with zero in the whole kinematic region $|t| > 0$ GeV^2. The results are compared with theoretical models and previous experiments.

Contents

1 Introduction

In order to study particle interactions and the creation of new particles, one uses scattering experiments. At the HERA[1] accelerator at DESY[2] in Hamburg, Germany, high-energetic leptons (electrons or positrons[3]) and protons are collided. A virtual photon mediates the electromagnetic interaction between the particles. When the momentum transfer to the photon is large, the proton constituents can be resolved and we speak of deep inelastic scattering (DIS). In the case of low momentum transfer, the photon is (quasi)real and we speak of *photoproduction*. The photon can fluctuate into a quark-antiquark pair interacting strongly with the proton. The result of the interaction is, in the case of photoproduction, a vector meson having the same quantum numbers ($J^{PC} = 1^{--}$) as the photon. Through photoproduction, the hadronic properties of the photon can therefore be probed.
An interesting aspect of this interaction is how the *helicity* of the photon is correlated with that of the vector meson. A natural starting point would be to assume that the helicity of the photon coincides with the one of the vector meson, so called S-Channel Helicity Conservation (SCHC). This assumption is based on the fact that electrons obey SCHC when scattered in a Coulomb field [1] and that this would be a general property of diffractive scattering as suggested by Gilman *et al.* [2]. A number of experiments have however shown that the helicity may very well be flipped, or even double-flipped, which hereafter is referred to as S-Channel Helicity Non-Conservation (SCHNC).

Already in 1973 Ballam *et al.* [3] studied photoproduction of ρ mesons by exposing the hydrogen LBL-SLAC bubble chamber to polarized photons. They found that the helicity to a high degree is conserved in the $\gamma \rightarrow \rho^0$ transistion. In 1998, the ZEUS collaboration presented a measurement [4] of the helicity properties of ρ in photoproduction at HERA. The analysis was done in the region of low transfered momentum t ($|t| < 0.5$ GeV^2) and the results showed consistency with SCHC. In 2000, the same collaboration presented an analysis [5] of diffractive photoproduction with large momentum transfer. Here, non-zero results for single- and double-flip amplitudes, implying deviations from SCHC, were presented. In an analysis based on the 2000 H1 data, Gwilliam *et al.* [6] investigated photoproduction of ρ with $|t| > 1$ GeV^2 and showed helicity violation. The data in this analysis is also from the H1 experiment at the HERA accelerator, but from the year 2005. Because of the efficient Fast Track Trigger [7] available since this year, the number of selected events at hand for this analysis is about 330 000, corresponding to a luminosity of 570 nb^{-1}. This makes it possible to look into kinematic regions never before observed with enough statistic. Especially the low-t region is interesting since perturbatice QCD (pQCD) is not applicable there.

The thesis is structured as follows. An overview of DESY, HERA and the H1 experiment is given in chapter 2. In chapter 3 the necessary theory is presented before a complete description of the analysis is made in chapter 4. The results are given and discussed in chapter 5 and the work is summarized in chapter 6.

[1] Hadron Electron Ring Accelerator
[2] Deutsches Elektronen-Synchrotron
[3] From now on in this thesis electron is used as notation for both electrons and positrons.

2 Experimental overview

DESY is one of the worlds leading facilities for high energy physics. It is located in Hamburg, Germany, and was founded in 1959. After many years of succesful experiments with electron-positron storage rings, the construction of HERA was started in 1984. Eight years later this first ever electron-proton collider was operationally ready and the collection of data from ep collisions could begin.

2.1 The HERA Accelerator

Situated 20 meters under ground, the HERA accelerator consists of two storage rings, each with a circumfence of 6.3 km. One of the rings is used for the proton and the other for the electron beam. The beam energy is 920 GeV for the protons and 27.5 GeV for the electrons resulting in a center of mass energy of $\sqrt{s} = 318$ GeV. The beams are collided where the two detectors ZEUS and H1 are situated. The proton (electron) bunches contain up to 10^{11} particles. In operational mode, about 180 bunches circulate in the storage rings in 96 ns intervals. At the fixed target experiment HERMES only the electron beam is used and collides with a fixed gas target[4]. A schematic overview of the accelerator is given in figure 1.

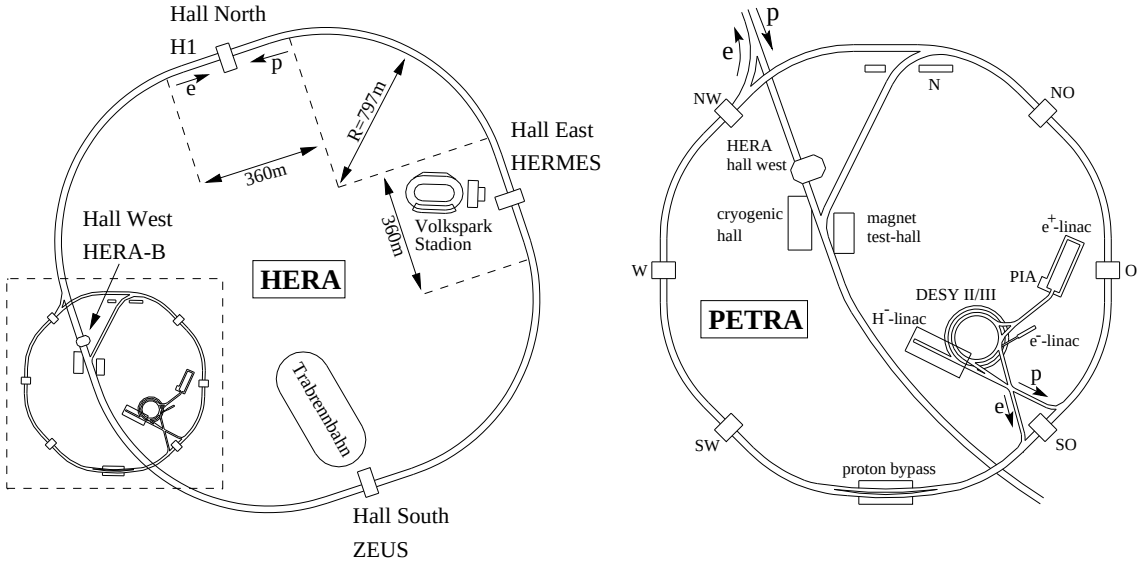

Figure 1: The HERA accelerator to the left and the storage ring PETRA, used for pre-acceleration, to the right.

2.2 The H1 Detector

Located in the HERA north hall, the H1 detector is a very large and complex system aimed to study the particles created when high energetic protons and electrons collide. It was built and is maintained by about 400 scientists from 39 institutes in 12 countries. A detailed describtion of the H1 detector can be found in [8]. Here the parts relevant for this thesis will be described.

[4]The now closed HERA-B experiment was also a fixed target experiment using the proton beam.

The H1 detector, unlike many other high energy physics detectors, is not a symmetric system. The reason is the large difference in energy between the proton and electron beam giving the total system a boost in the forward (proton) direction. This direction is therefore also chosen as the positive z-direction for the H1 coordinate system. The x-axis points towards the center of the ring and the y-axis points upwards, together spanning the transverse detector plane. Two angles of importance are introduced; the polar angle θ between the particle trajectory and the positive z-axis and the azimuthal angle ϕ between the trajectory and the positive x-axis in the transverse plane. The relation between the angle θ and the *pseudo-rapidity* η is given by

$$\eta = -\ln(\tan\frac{\theta}{2}). \tag{1}$$

In figure 2 a schematic picture of the detector is presented. The electron and proton beams collide in the interaction zone of the beam pipe and produce new particles. These new particles are detected through different sub-detectors surrounding the interaction point. The particle tracks are measured by the central *tracking system*, consisting of the two central jet chambers CJC1 and CJC2 (2 in the figure), the inner multi wire proportional chamber CIP, the outer z vertex chamber COZ, the outer multi wire proportional chamber COP and the silicon vertex detector CST. The H1 tracking detectors are surrounded by *calorimeters*: in the forward and central region by a liquid argon calorimeter for electromagnetic 4 and hadronic 5 showers respectively. To measure the scattered electron, a scintillating fibre spaghetti calorimeter (SpaCal) is installed in the backward region 12. Muons and high energetic hadrons passing the calorimeters are detected in the *muon system* consisting of an instrumented iron return yoke (Central Muon Detector 10) and a Forward Muon Detector 11. To determine the luminosity the high energy photon from the bremsstrahlung reaction $ep \to ep\gamma$ is detected in a lead-scintillator calorimeter located at $z = -103$ m in the HERA tunnel.

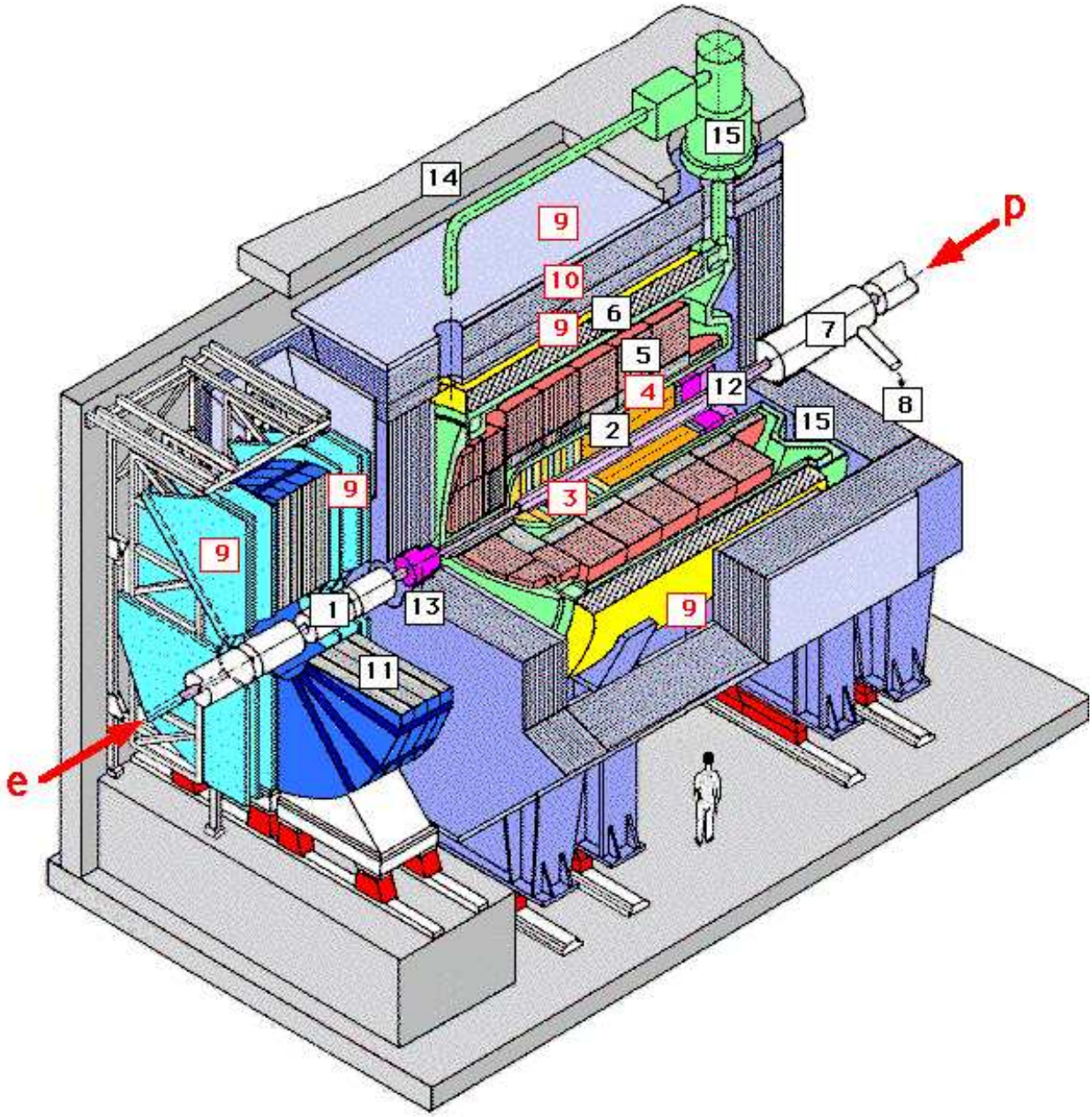

Figure 2: The H1 detector with its main components: 1 Beam pipe and beam magnets, 2 Central tracking detector, 3 Forward tracking detector, 4 Electromagnetic LAr calorimeter, 5 Hadronic LAr calorimeter, 6 Superconducting coil (1.15 T), 7 Compensating magnet, 8 Helium supply for 7, 9 Muon chambers, 10 Instrumented iron yoke, 11 Forward muon toroid, 12 Scintillating fibre spaghetti calorimeter (SpaCal), 13 PLUG calorimeter, 14 Concrete shielding, 15 Liquid argon cryostat

2.2.1 Triggering

In 2001, a major upgrade of HERA was performed. By adding superconducting focusing magnets the luminosity was increased by a factor of five. To be able to handle the increased rates of both signal and background a more efficient event triggering (filtering and selection) was needed. The so called *Fast Track Trigger* (FTT) system was developed by the H1 Collaboration and since it is essential for the analysis, it will be described more carefully here. The system is motivated by the fact that the ep collision rate is about 1 kHz (the background beeing 10 to 100 times higher) whereas only five to ten events per second can be written to tape [9]. A full description of the FTT can be found in [7].

- **The FTT system**

The FTT system is used to trigger interesting physics events and separate these events from the background. The information to the FTT comes from the CJC and as can be seen in figure 3, three trigger *layers* in CJC1 and one layer in CJC2 are used. What is refered to as one trigger layer consists of three nearby layers of wires.

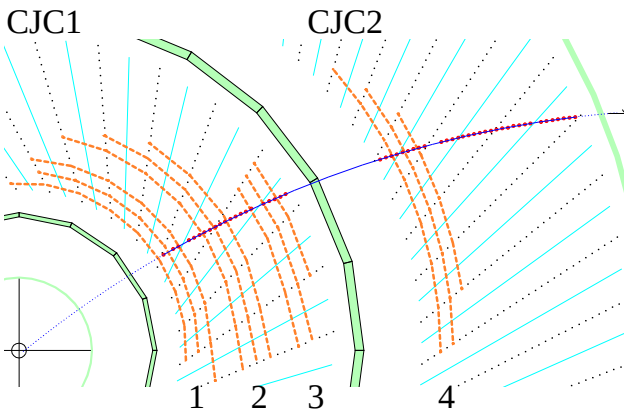

Figure 3: A rϕ-view of the detector showing the CJC with the four wire layers.

The information from the trigger layers is input to four different trigger *levels* where track fitting and calculation of kinematic variables are performed. Level 1 (L1) is a dead time free hardware trigger with a decision time of 2.3μs used to find track segments. The output pattern from the trigger layers are compared with different masks in order to identify tracks. The different masks are stored in so called Content Addressable Memories (CAM) which is basically an inverse RAM since the input is compared with the patterns giving the memory adress to the pattern as output. The number of masks is enough [9] to identify all tracks with $p_t > 100$ MeV. At Level 2 (L2) the information from L1 is refined. The tracks have to be fitted within 20μs and in this period of time parameters like momentum sums and invariant masses are determined for low multiplicity events. Finally, the parameters from the fitted tracks are sent to L3 where a full search for resonances is performed. This has to be performed within 100μs and the final L3 decision may also take other detector parts into account. Events are then sent and buffered at a filter farm (L4) where they are fully

reconstructed within 100 ms. The FTT allows a reconstruction of three dimensional tracks down to 100 MeV in the L2 latency 20μs. By using advanced reconstruction algorithms the goal of a momentum resolution of 5% (at $p_t = 1$ GeV) is achieved.

3 Theory

3.1 Kinematics in ep collisions

In the scattering of electrons on protons at HERA, the electromagnetic coupling is small and the basic process

$$e(k) + p(P) \rightarrow e(k') + X \tag{2}$$

can be approximated with a one-photon-exchange at low momentum transfer. With the four-vector of respective particle given in parenthesis, the generic diagram for the reaction is

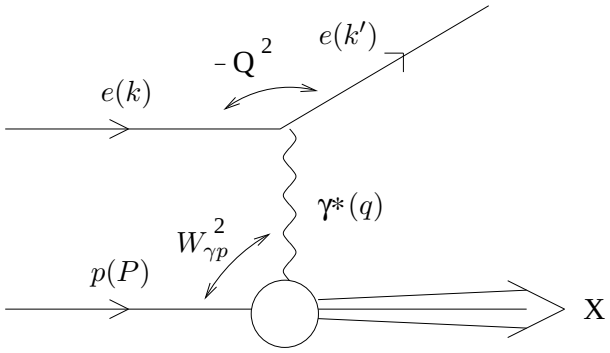

Figure 4: The general ep scattering event.

For this process the fundamental kinematic variables are

$Q^2 = -(k - k')^2 = -q^2$, the modulus of the squared four-momentum of the virtual photon

$W_{\gamma p} = (q+P)^2 = 2m_p\nu + {m_p}^2 - Q^2$, the squared center-of-mass for the photon-proton system. In the last expression, valid in the proton rest system, the additional variable $\nu \equiv \frac{P \cdot q}{m_p}$ was introduced.

$y = \frac{q \cdot P}{k \cdot P}$, the fraction of the electron energy transferred to the photon, as seen in the proton rest frame

$x = \frac{Q^2}{2P \cdot q}$, the Bjorken variable which for large Q^2 is interpreted as the fraction of the proton's longitudinal momentum carried by the struck parton

The experimental definition is that for $Q^2 > 4$ GeV^2 it is deep inelastic scattering (DIS) whereas for $Q^2 < 4$ GeV^2 it is photoproduction.

3.2 Photoproduction of vector mesons

In ep collisions with low Q^2, the electron scatters on the proton at small angles. Because of the low Q^2, the photon exchanged between the electron and the proton is (quasi)real and we can think of a proton-photon scattering process with the electron simply acting as a photon source. In the photoproduction of vector mesons, the photon fluctuates into a $q\overline{q}$-pair, which in turn interacts strongly with the proton to produce a bound, on-mass-shell state of a quark and an anti-quark. This bound state is a meson and since conservation of charge demands production of a neutral vector meson, $\rho, \phi, \omega, J/\psi$ or higher resonances of these particles are possible. The general expression for photoproduction of a vector meson is given in equation (3) below.

$$e(k) + p(P) \rightarrow e'(k') + V(v) + X(P') \tag{3}$$

Here k (k') is the 4-vector of the electron before (after) collision, P is the 4-vector of the proton, v of the vector meson and P' of X. The X denotes a final state which can be a complex hadronic state, a so called proton remnant, in the dissociative case or the scattered proton in the elastic case. These two final states are visualized in figure 5.

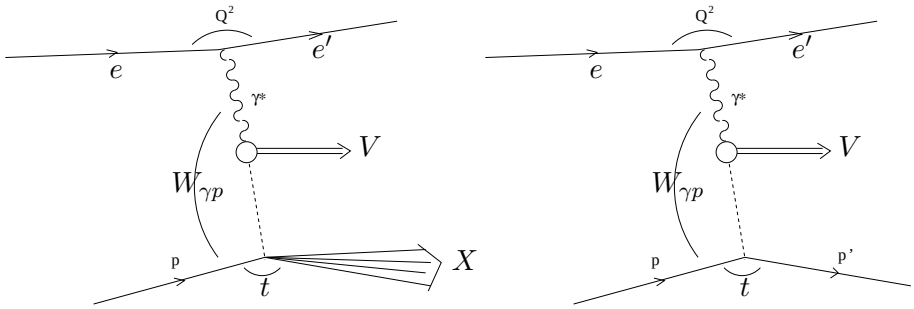

Figure 5: Photoproduction with two different final states, the dissociative case to the left and the elastic one to the right.

In figure 5, the kinematic variables of particular interest for photoproduction are presented. The virtuality of the photon, Q^2, has been introduced in section 3.1. The transfered four-momentum t can be defined for special events and in photoproduction, where Q^2 is small, it can be approximated according to

$$t = (P - P')^2 = (v - q)^2 \approx -{p_{t,v}}^2 \tag{4}$$

where p_t is the transverse momentum of the vector meson. In figure 5, the invariant mass, denoted $W_{\gamma p}$, of the photon-proton system is also to be seen.

3.2.1 Perturbative QCD models

In the region of high $|t|$, pQCD can be used to model the diffractive vector meson production. It is assumed that the hard interaction between the $q\overline{q}$ pair and the proton is mediated either

by two gluons at Leading Order (LO) [10, 11, 12, 13] or by a gluon ladder described by the Leading Logarithm (LL) BFKL evolution equation [10, 13, 14, 15]. Poludniowski *et al.* [16] have obtained a complete solution of the non-forward ($t \neq 0$) BFKL equation and, for the first time, analytical solutions for the BFKL evolved scattering amplitudes were presented for all helicity combinations.

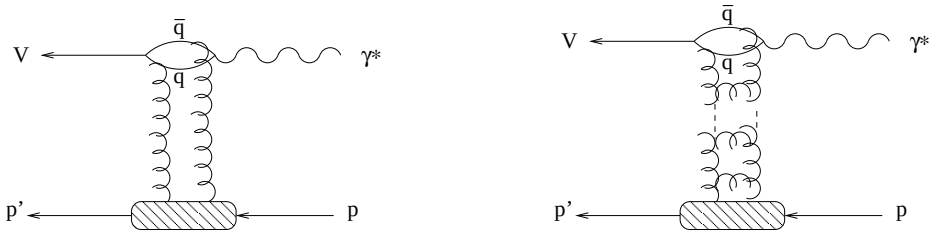

Figure 6: The pertubative QCD models describing photoproduction of vector mesons. To the left the two-gluon exchange and to the right the gluon ladder described by the BFKL evolution equation.

3.2.2 The Pomeron

In the soft region (small $|t|$ and Q^2) perturbative QCD (pQCD) is not applicable. As first described by Pomeranchuk, the elastic scattering is dominated by a vacuum exchange in the t-channel viewpoint. In 1961 Chew and Frautschi conjectured that the vacuum channel can be described by a C-even, isoscalar, positive parity reggeon. This reggeon was first called the Pomeranchukon but soon shortened to the *Pomeron*. The processes pictured in 5 are described with Pomeron exchange. For more information about the early history of the Pomeron see [17].

3.2.3 Cross section

The pomeron is actually not a particle but rather a trajectory describing how the total cross section for the diffractive vector meson production depends on the kinematic variable W. The energy dependence for the elastic cross section is given by

$$\frac{d\sigma^{elas}}{dt} \propto W^{4(\alpha(t)-1)} \tag{5}$$

where α is a t-dependent parameter specific to the exchanged Regge trajectory. When studying the cross section both the elastic and proton dissociative defined in section 3.2 have to be included. They have however different t-dependences, the elastic process dominates in the low-t region and the proton dissociative process in the high-t region.

The cross section for a physical process can experimentally be determined by correcting and normalizing the event distribution. In this thesis no absolute cross section is determined. The shape of the event distribution is enough and therefore normalization constants like the photon flux will not be calculated. The corrections for acceptance and efficiency have however to be applied in order to get the correct mass shape. This motivates the correction procedure described in section 4.8.

3.3 Angular distribution

3.3.1 Helicity angles

In the general case, three helicity angles are needed to describe photoproduction of a vector meson and its decay into two lighter mesons. In photoproduction at HERA, the scattered electron is not observed and the angle Φ between the vector meson production plane and the electron scatttering plane is therefore not accessible. In this report, all expressions for angular distributions therefore apply to the special case where Φ is unobserved[5] . The two remaining angles are ϕ^*, the angle between the vector meson production plane and its decay plane, and θ^*, the azimuthal angle for the positive pion as seen in the rest frame of the vector meson. These angles are visualized in figure 7.

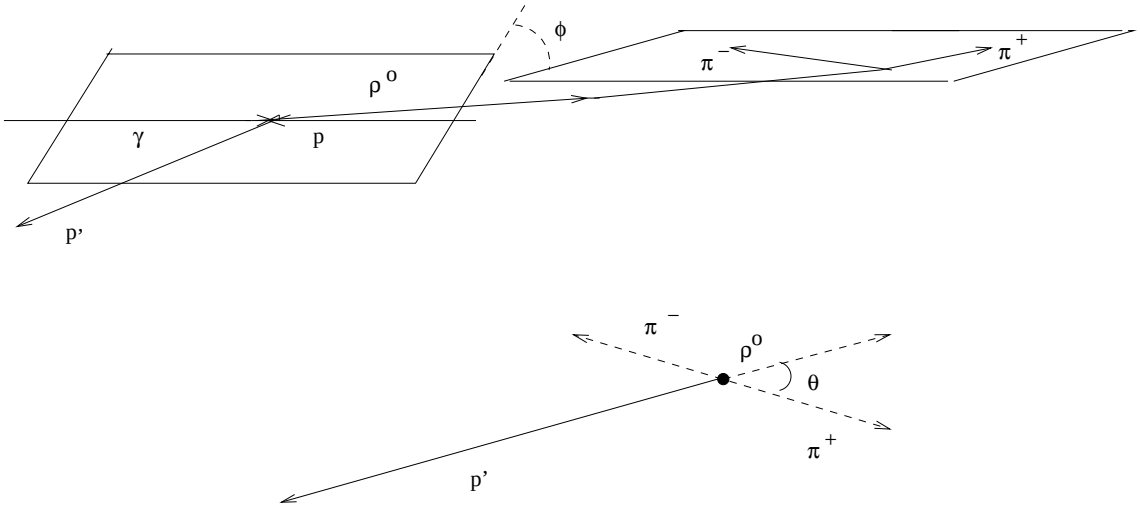

Figure 7: The helicity angles ϕ^* and θ^*.

3.3.2 Calculation of helicity angles

If the four-momentum of the incoming photon and outgoing vector meson in the γp center-of-mass system are denoted with v and q, the corresponding three vectors $\vec{v}$ and $\vec{q}$ can be used to define a right-handed coordinate system [18]

$$\hat{z} = \frac{\vec{v}}{|\vec{v}|}, \quad \hat{y} = \frac{\vec{v} \times \vec{q}}{|\vec{v} \times \vec{q}|}, \quad \hat{x} = \frac{(\vec{v} \times \vec{q}) \times \vec{v}}{|(\vec{v} \times \vec{q}) \times \vec{v}|} \tag{6}$$

With $\vec{\pi}$ being the three vector of the positive pion in the rest frame of the vector meson, the two helicity angles can be calculated from

$$\cos\theta^* = \frac{\vec{\pi} \cdot \vec{z}}{|\vec{\pi} \cdot \vec{z}|} \tag{7}$$

$$\cos\phi^* = \frac{\vec{y} \cdot (\vec{z} \times \vec{\pi})}{|\vec{z} \times \vec{\pi}|}, \quad \sin\phi^* = -\frac{\vec{x} \cdot (\vec{z} \times \vec{\pi})}{|\vec{z} \times \vec{\pi}|} \tag{8}$$

[5]See for instance [18] for a full description.

3.3.3 Parametrization of the angular distribution

The cross section for the reaction in equation (3) and the ρ decay into two pions can be parametrized with the helicity angles ϕ^* and θ^*, the photon density matrix elements $\rho_{\lambda\lambda'}$ and the helicity amplitudes $M_{\lambda_\gamma\lambda_V}$ [18]. Here $M_{\lambda_\gamma\lambda_V}$ $(\lambda_\gamma, \lambda_V = -, 0, +)$ is the amplitude describing how a vector meson of helicity λ_V is photoproduced from a photon with helicity λ_γ. A more natural parametrization for this analysis is however to use the spin density matrix elements for the vector meson together with the helicity angles. The spin density matrix elements are denoted r^α_{ij} $(ij = -1, 0, +1)$ and describe the interference between a vector meson with helicity λ and one with λ'. α describe the photon helicities interfering. Since the angle Φ is not accessed in this analysis, all terms contributing are diagonal in photon helicity. This is denoted by the superscript 04. The result for the angular distribution is

$$\begin{aligned}\frac{1}{\sigma}\frac{d\sigma}{d\cos\theta^* d\phi^*} &= \frac{3}{4\pi}[\frac{1}{2}(1-r^{04}_{00}) + \frac{1}{2}(3r^{04}_{00}-1)\cos^2(\theta^*) - \\ &\quad - \sqrt{2}\mathrm{Re}\{r^{04}_{10}\}\sin(2\theta^*)\cos(\phi^*) - r^{04}_{1-1}\sin^2(\theta^*)\cos(2\phi^*)] \end{aligned} \tag{9}$$

It is also of interest to study not only the two dimensional distribution in (9) but also the one dimensional ones for $\cos\theta^*$ and ϕ^*. Intergrating (9) over ϕ^* gives

$$\frac{d\sigma}{d\cos\theta^*} \propto 1 - r^{04}_{00} + (3r^{04}_{00}-1)\cos^2(\theta^*) \tag{10}$$

whereas an intergration of (9) over $\cos\theta^*$ gives

$$\frac{d\sigma}{d\phi^*} \propto 1 - 2r^{04}_{1-1}\cos(2\phi^*) \tag{11}$$

The relations between the r_{ij} and the $M_{\lambda_\gamma\lambda_V}$ are in the general case given by

$$r^{04}_{00} \propto \epsilon|M_{00}|^2 + |M_{+0}|^2 \tag{12}$$

$$\mathrm{Re}\{r^{04}_{10}\} \propto \frac{1}{2}\mathrm{Re}\{M_{++}M^*_{+0}\} + \epsilon\mathrm{Re}\{M_{0+}M^*_{00}\} + \frac{1}{2}\mathrm{Re}\{M_{-+}M^*_{-0}\} \tag{13}$$

$$r^{04}_{1-1} \propto -\epsilon|M_{0+}|^2 + \mathrm{Re}\{M_{++}M^*_{-+}\} \tag{14}$$

where ϵ is the longitudinal polarization of the photon given by

$$\epsilon \equiv \frac{1 - y - y^2\frac{Q^2}{4\nu^2}}{1 - y + \frac{1}{2}y^2 + y^2\frac{Q^2}{4\nu^2}} \approx \frac{2(1-y)}{(1-y)^2+1} \tag{15}$$

The approximate expression is given in [19] and is valid for small-x and is appropriate for DIS events at HERA.

(12)-(14) are the general expressions where the virtuality of the photon, proportional to the polarization ϵ is taken to be non-zero. An important special case of these equations is

when the longitudinal polarization of the photon is negligible which is, to a very good approximation, the case in the kinematic region $Q^2 < 0.01$ GeV^2. Under this assumption, the relations read

$$r_{00}^{04} = \frac{|M_{+0}|^2}{|M_{++}|^2 + |M_{+0}|^2 + |M_{+-}|^2} \quad (16)$$

$$\mathrm{Re}[r_{10}^{04}] = \frac{1}{2}\frac{M_{++}M_{+0}^* - M_{+-}M_{+0}^*}{|M_{++}|^2 + |M_{+0}|^2 + |M_{+-}|^2} \quad (17)$$

$$r_{1-1}^{04} = \frac{1}{2}\frac{M_{++}M_{+-}^* + M_{+-}M_{++}^*}{|M_{++}|^2 + |M_{+0}|^2 + |M_{+-}|^2} \quad (18)$$

It should be mentioned that there are also amplitudes M_{-+}, M_{-0} and M_{--} describing ρ production from a photon with negative helicity. Since these amplitudes are not independent and satisfy $M_{--} = M_{++}$, $M_{+-} = M_{-+}$ and $M_{+0} = M_{-0}$ [6] they are not stated explicity in the formulae above.

3.3.4 Angular distribution in the SCHC approximation

The helicity of the incoming photon coincides with that of the outgoing vector meson in the diffractive cone as shown in [19]. It is therefore a natural starting point to assume SCHC. If the vector meson carries over the helicity of the photon, the only non-zero amplitudes are M_{++} and M_{00} which for (12)-(14) gives

$$r_{00}^{04} \propto \epsilon|M_{00}|^2 \quad (19)$$

$$\mathrm{Re}[r_{10}^{04}] = 0 \quad (20)$$

$$r_{1-1}^{04} = 0 \quad (21)$$

In the limit where the longitudinal polarization of the photon is negligible, the matrix elements under the assumption of SCHC are all equal to zero.

$$r_{00}^{04} = 0 \quad (22)$$

$$\mathrm{Re}[r_{10}^{04}] = 0 \quad (23)$$

$$r_{1-1}^{04} = 0 \quad (24)$$

With all matrix elements equal to zero, the angular distribution takes the following simple form

$$\frac{1}{\sigma}\frac{d\sigma}{d\cos\theta^* d\phi^*} = \frac{3}{4\pi}\frac{1}{2}[1 - \cos^2(\theta^*)] \quad (25)$$

3.3.5 Formal derivation of the matrix elements

A general quantum mechanical state, being the superposition of three helicity states, is

$$|\Phi> \quad = \quad \alpha \cdot |+> \quad + \quad \beta \cdot |0> \quad + \quad \gamma \cdot |-> \tag{26}$$

The coefficients α, β, γ corresponds in this analysis to the amplitudes M_{++}, M_{+0}, M_{+-} and the density matrix can now be evaluated

$$r_{ij} = |\Phi><\Phi| =$$

$$\begin{aligned} &= \frac{1}{\sqrt{N}} \quad (M_{++} \cdot |+> \quad + \quad M_{+0} \cdot |0> \quad + \quad M_{+-} \cdot |->) \cdot \\ &\quad \cdot \frac{1}{\sqrt{N}} \quad (<+| \cdot M^*_{++} \quad + \quad <0| \cdot M^*_{+0} \quad + \quad <-| \cdot M^*_{+-}) \quad = \end{aligned}$$

$$= \frac{1}{N} \begin{pmatrix} |M_{++}|^2 & M_{++}M^*_{+0} & M_{++}M^*_{+-} \\ M_{+0}M^*_{++} & |M_{+0}|^2 & M_{+0}M^*_{+-} \\ M_{+-}M^*_{++} & M_{+-}M^*_{+0} & |M_{+-}|^2 \end{pmatrix} \equiv \begin{pmatrix} r_{11} & r_{10} & r_{1-1} \\ r_{01} & r_{00} & r_{0-1} \\ r_{-11} & r_{-10} & r_{-1-1} \end{pmatrix} \tag{27}$$

Conservation of parity is valid and this reduces the number of independent matrix elements according to [18]

$$r_{ij} = (-1)^{i-j} r_{-i-j} \tag{28}$$

giving the following relations between the matrix elements[6]

$$r_{11} = (-1)^{1-1} r_{-1-1} = r_{-1-1} \tag{29}$$
$$r_{10} = (-1)^{1-0} r_{-10} = -r_{-10} \tag{30}$$
$$r_{01} = (-1)^{0-1} r_{0-1} = -r_{0-1} \tag{31}$$
$$r_{1-1} = (-1)^{1+1} r_{-11} = r_{-11} \tag{32}$$

Since r_{ij} is a hermitian matrix (satisfying $r_{ij} = \overline{r}_{ji}$) some additional relations can be stated

$$r_{00} = \overline{r}_{00} \quad \Rightarrow \quad r_{00} \in \mathbf{R} \tag{33}$$

$$r_{\pm 1 \pm 1} = \overline{r}_{\pm 1 \pm 1} \quad \Rightarrow \quad r_{\pm 1 \pm 1} \in \mathbf{R} \tag{34}$$

$$r_{10} = \overline{r}_{01} \tag{35}$$

$$r_{1-1} = \overline{r}_{-11} \tag{36}$$

[6]For simplicity the superscript 04 has overall been left out in this derivation.

For r_{00}, for instance, one gets by direct comparison in (27)

$$r_{00} = \frac{1}{N}|M_{+0}|^2 \tag{37}$$

which is consistent with equation (16). For $\mathrm{Re}[r_{10}]$ (31) gives

$$r_{10} = -r_{-10} \quad \Rightarrow \quad r_{10} + r_{0-1} = 0 \tag{38}$$

Taking the complex conjugate of r_{0-1} gives, when subtracting the two matrix elements

$$r_{10} - \overline{r}_{0-1} = 2 \cdot \mathrm{Re}[r_{10}] \quad \Rightarrow \quad \mathrm{Re}[r_{10}] = \frac{1}{2}(r_{10} - \overline{r}_{0-1}) \tag{39}$$

Expressing the matrix elements with the amplitudes from the matrix in (27) the result is

$$\mathrm{Re}[r_{10}] = \frac{1}{2}\frac{M_{++}M^*_{+0} - (M_{+0}M^*_{+-})^*}{N} = \frac{1}{2}\frac{M_{++}M^*_{+0} - M_{+-}M^*_{+0}}{N} \tag{40}$$

which is consistent with the expression in (17).

Finally, r_{1-1} has to be real as can be seen from (32) and (36). Because of the hermicity one can directly express the matrix element with the transistion amplitudes ending up with the result in equation (18)

$$r_{1-1} = \frac{1}{2}\frac{M_{++}M^*_{+-} + (M_{++}M^*_{+-})^*}{N} = \frac{1}{2}\frac{M_{++}M^*_{+-} + M_{+-}M^*_{++}}{N} \tag{41}$$

3.3.6 Expected results for the matrix elements

Since the spin density matrix must be unitary, the absolute value of respective matrix element has to satisfy

$$|r_{ij}| \leq 1 \tag{42}$$

In [18], Schilling *et al.* go further and derive inequalities for the spin density matrix elements. For the ones relevant for this analysis the results are

$$0 \leq r^{04}_{00} \leq 1 \tag{43}$$

$$|r^{04}_{1-1}| \leq \frac{1}{2}(1 - r^{04}_{00}) \tag{44}$$

$$(\mathrm{Re}\{r^{04}_{10}\})^2 \leq \frac{1}{4}r^{04}_{00}(2 - r^{04}_{00} - \mathrm{Re}\{r^{04}_{10}\}) \tag{45}$$

3.4 Physical picture

This section aims to get a better understanding of what the different matrix elements really mean. For simplicity this is made under the assumption of negligible longitudinal polarization. This means that photon is assumed to have positive helicity (as stated in chapter 3.3.3 the amplitudes where the photon has negative helicity are not independent).
r_{ij} is a spin density matrix and all the diagonal elements are proportional to the probability of finding a certain quantum mechanical state. r_{00}^{04} therefore means the probability of finding a vector meson with helicity zero. Under the assumption of positive photon helicity stated above, the only amplitude contributing is M_{+0}. It is therefore intuitive that r_{00}^{04} is defined as in (16)

$$r_{00}^{04} = \frac{|M_{+0}|^2}{|M_{++}|^2 + |M_{+0}|^2 + |M_{+-}|^2}$$

The off-diagonal terms do not directly represent the probability of being in a certain state but are so called interference terms. One can study r_{1-1}^{04} as an example. This matrix element means interference of processes where the vector meson has helicity $+1$ or -1. Production of a helicity $+1$ vector meson is proportional to M_{++} and one with helicity -1 to M_{+-}. Taking also the hermitican conjugate, motivated by the derivation in section 3.3.5, one ends up with (18).

$$\mathrm{Re}[r_{10}^{04}] = \frac{1}{2}\frac{M_{++}M_{+0}^{*} - M_{+-}M_{+0}^{*}}{|M_{++}|^2 + |M_{+0}|^2 + |M_{+-}|^2}$$

The same type of reasoning can be applied to $\mathrm{Re}[r_{10}^{04}]$ making equation (17)

$$r_{1-1}^{04} = \frac{1}{2}\frac{M_{++}M_{+-}^{*} + M_{+-}M_{++}^{*}}{|M_{++}|^2 + |M_{+0}|^2 + |M_{+-}|^2}$$

plausible. In figure 8-10 the processes contributing to each matrix element are visualized.

It is also interesting to study what helicity violation in photoproduction really mean [19]. From the point of view of pQCD the transistion of the photon to the $q\overline{q}$-pair is described by the QED vertex $e\overline{q}\gamma_\mu q A_\mu$. A longitudinal (scalar) virtual photon with helicity $\lambda_\gamma = 0$ consists of a $q\overline{q}$ Fock state with $\lambda + \overline{\lambda} = 0$. The crucial point is that a transverse photon with helicity $\lambda_\gamma = \pm 1$ not only consists of $q\overline{q}$ states with $\lambda + \overline{\lambda} = \pm 1$ but also a state $\lambda + \overline{\lambda} = 0$ where the photon helicity is carried by the orbital angular momentum of the quarks. Since the transverse and longitudinal photons share the state with $\lambda + \overline{\lambda} = 0$ s-channel helicity violating transitions from transverse (longitudinal) photons to longitudinal (transverse) vector mesons are allowed.

- The matrix element r_{00}^{04}

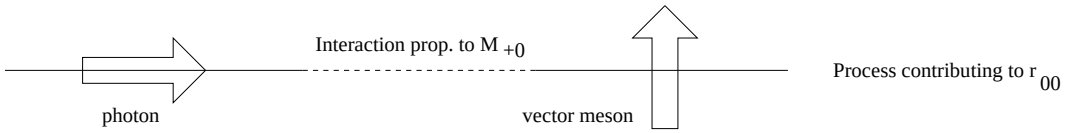

Figure 8: This is the only process contributing to r_{00}^{04} since this matrix element means production of a vector meson with helicity zero.

- The matrix element $\mathrm{Re}[r_{10}^{04}]$

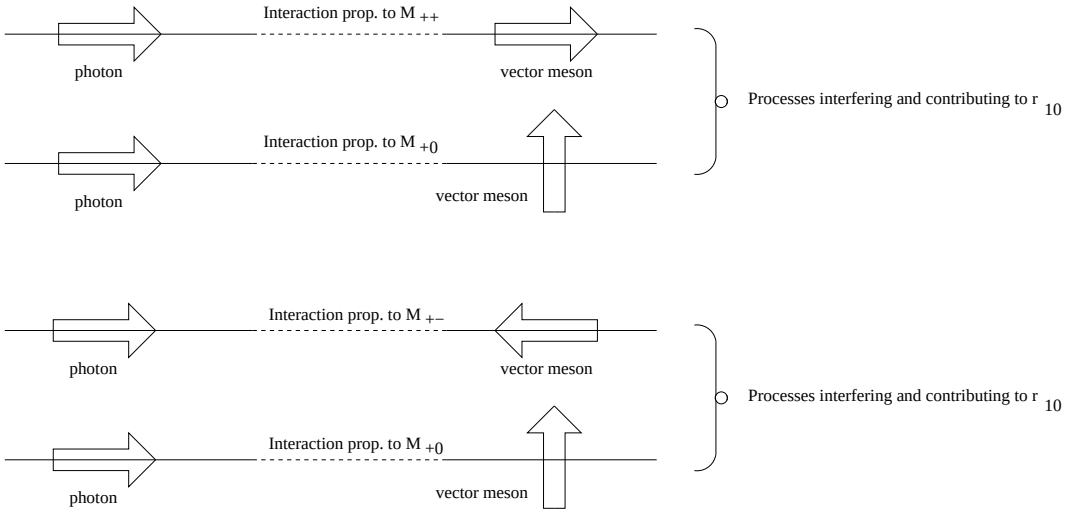

Figure 9: $\mathrm{Re}[r_{10}^{04}]$ is a sum of the two interference terms. The two processes above give one interference term and the two below give the other.

- The matrix element r_{1-1}^{04}

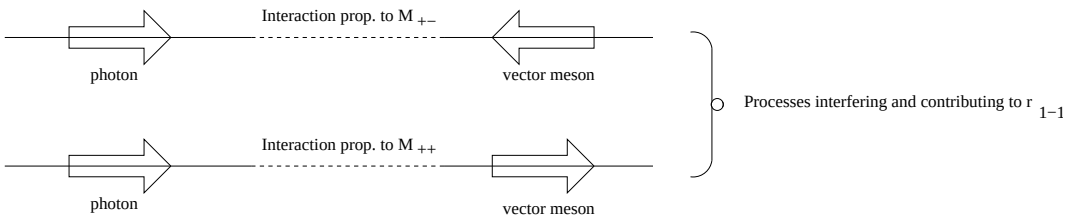

Figure 10: This process together with its hermitian conjugate contribute to r_{1-1}^{04}.

4 Data analysis

4.1 Overview

The goal of this analysis is to determine the spin density matrix elements, given by (16)-(18), for ρ from photoproduction at HERA. This is done by determining the angular distribution for ρ production and decay into π^+ and π^-

$$p + \gamma^* \rightarrow p' + \rho \rightarrow p' + \pi^+ + \pi^- \tag{46}$$

Since the branching ratio for the ρ decay into two pions is almost 100%, this is the only decay channel investigated. The angular distribution, parametrized by the two helicity angles θ^* and ϕ^*, depends on the spin density matrix elements r_{ij}. These matrix elements can therefore be accessed by fitting the angular distribution to the theoretical models, the two-dimenional (9) and the one-dimensional (10)-(11) functions.

4.2 Data

The analysis is based on the data collected by the H1 experiment in the year 2005 where an electron beam was used. The data set includes almost 1 million events and corresponds to a luminosity of 570 nb^{-1}. The data was collected according to

- FTT, subtrigger 14
  Run range: 421402 - 427934

In the HERA run 2005 a large set of ep triggers were installed, each defined to trigger a certain physical process in the ep collision. To pick out the events used in this analysis, the *subtrigger 14* was used. It was one of first subtriggers for physics using the FTT and is described in more details in section 4.2.1.

4.2.1 Subtrigger 14

The definition of the subtrigger is

```
s14: FTT_mul_Tb>1 && FTT_mul_Ta<4 && FTT_chg_1 && (!LAr_IF) && CIP_sig>2 &&
     CIP_mul<6   v:5 t:0 d:1
```

The different trigger elements are

- `FTT_mul_Tb>1 && FTT_mul_Ta<4`
  `FTT_mul_Ta` is the number of tracks with transverse momentum $p_t > 100$ MeV and `FTT_mul_Tb` the number of tracks with $p_t > 160$ MeV. To summarize, two or three tracks are demanded, all of them with $p_t > 100$ MeV and with at least two track having $p_t > 160$ MeV.

- `FTT_chg_1`
  This abbreviation means `FTT_Qtot>2 && FTT_Qtot<6` and is explained through table 1. As can be seen, if `FTT_chg_1` is to be fullfilled, we demand that the total charge of the tracks has to fullfill $-2 < Q_{tracks} < +2$.

FTT_Qtot	0	1	2	3	4	5	6	7
charge	nan	<-3	-2	-1	0	+1	+2	>+3

Table 1: The different values that can be applied to select the total charge of the tracks.

- `(!LAr_IF)`
  A so called veto making sure that no activity in the forward liquid argon calorimeter is seen. This is a cut against inelastic events.

- `CIP_sig>2`
  This is the significance of the central peak in a zvtx histogram and is defined as $n(cen) > k \cdot [n(fwd) + n(bwd)]$. One has CIP_sig(k)= 1(k=1) 2(k=2) 3(k=4).

- `CIP_mul<6`
  This is the CIP Multiplicity giving the number of tracks calculated as the sum of central, forward and backward tracks. With `CIP_mul<6` this number satisfies $0 \leq n \leq 30$.

- `v:5 t:0 d:1`
  These global options are used to supress the background processes.

4.3 Reconstruction of the ρ candidate

From each triggered event, the ρ candidate is reconstructed. Since the ρ meson decays almost instantaneously (the decay time is about 10^{-24} s [20]) into a π^+ and a π^-, it is the pion tracks that are used for the reconstruction. The event topology is therefore characterized by

- Two tracks and no other tracking activity.

A typical event is shown with the H1 event display in figure 11. With the pion three momentum from the tracking chambers the four vectors can easily be reconstructed assuming pion masses. They are then used to calculate the four-vector of the ρ meson

$$p_\rho = p_{\pi^+} + p_{\pi^-} \tag{47}$$

The invariant mass of the ρ candidate can be calculated according to

$$M_{\pi\pi} = \sqrt{(E_{\pi^+} + E_{\pi^-})^2 - (\vec{p}_{\pi^+} + \vec{p}_{\pi^-})^2} \tag{48}$$

The t-value is calculated according to the approxiamtion in (4)

$$t \approx -{p_{t,\rho}}^2 \tag{49}$$

Instead of the expression presented in section 3.1 the Jacquet-Blondel method [21] is used to calculate the value of W

$$W = \sqrt{2 \cdot (E_\rho - p_{z,\rho}) \cdot E_p} \tag{50}$$

The reason is that to use (50) no information of the energy transfer from the electron to the photon is needed. The proton energy in (50) is known to be 920 GeV at HERA.

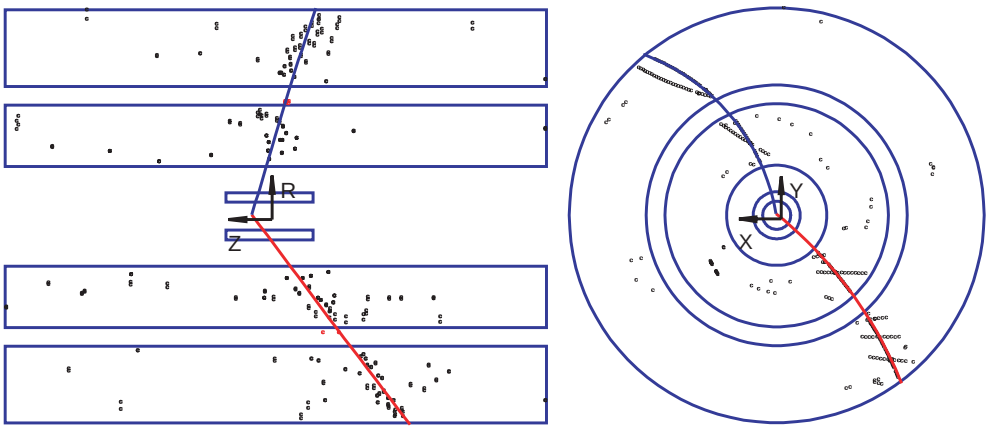

Figure 11: An event from the dataset pictured with the H1 Event Display. As can be seen the event topology is characterized by two tracks and no other tracking actitvity.

The Q^2 value is assumed to be small and is also neglected in the reconstruction of the other kinematic variables.

Finally the helicity angles for the event are calculated by boosting the pion vector to the rest system of the vector meson and then applying equations (7) and (8).

4.4 Event selection

From the set of triggered events, the good ρ candidates have to be selected. Below are listed the cuts used for this selection

- No scattered electron

Since the scattered electron is not observed, this is to make sure that no such track is present. This also picks out the low Q^2-region since the electron becomes detectable for larger Q-values.

- Vertex position

By restricting the z-coordiante (given in the H1 coordiante system defined in section 2.2) to $|z| < 25$ cm, regions where the CJC has low acceptance are rejected. This cut also surpresses the beam gas interaction background (described in section 4.6.1) since those events do not primarly come from the region around the interaction point at z=0.

- Tracking

Two *central tracks* are demanded. To make sure that events with exactely two tracks are selected all reconstructed tracks are counted and only events with two tracks pass the selection criteria. It is important to realize that when studying the two pion tracks coming from

the decaying ρ particle, it is not possible to resolve the distance travelled by the ρ before decaying. The total width Γ of the ρ is 150.3 ± 1.6 MeV [20]. This can be used to evaluate the decay time τ according to

$$\Gamma\tau \sim \hbar \tag{51}$$

Using the number for the width together with $\hbar = 6.6 \cdot 10^{-22}$ MeVs one gets

$$\tau \sim 4.4 \cdot 10^{-24} s \tag{52}$$

This decay time can, as in figure 12, be related to a distance travelled in the detector before decaying.

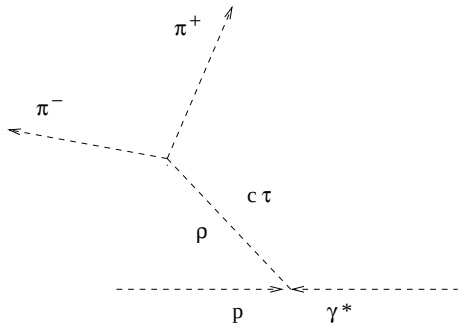

Figure 12: The decay length of the ρ meson is the distance travelled from the primary vertex until it decays into two pions.

Calculating this distance gives $c\tau \approx 10^{-15}$ m. The CST detector used for vertex fitting has a resolution of the order of 10^{-5} m [23] so it is not possible to resolve the flight distance of the ρ. The pion tracks are therefore considered to come from the primary interaction point.

- `20 <` θ_{track} `< 160 deg`

This cut restricts the angle between the beam and the track to a region where the central detector system has a high enough acceptance.

- Oppositely charged tracks

Since we know that the vector meson decays into two oppositely charged pions we demand opposite charge for the two tracks.

- `pt < 0.2 GeV`

Because the reconstruction efficency is low for low p_t we demand a minimum of 200 MeV of transverse momentum for each track. By studying figure 22, it is inferred that this cut only rejects a small amount of events.

- `0.6 <` $M_{\pi\pi}$ `< 1.1 GeV`

This cut is to pick out the ρ mass peak and to supress the background. The mass $M_{\pi\pi}$ is calculated according to (48) and can be compared with the average mass value 768.5 ± 1.1 MeV for ρ from photoproduction [20]. The peak in figure 13 is shifted to the right compared to this value. In the Söding model [22] this skewing of the mass peak is attributed to the interference between resonant and non-resonant production of $\pi^+\pi^-$-pairs.

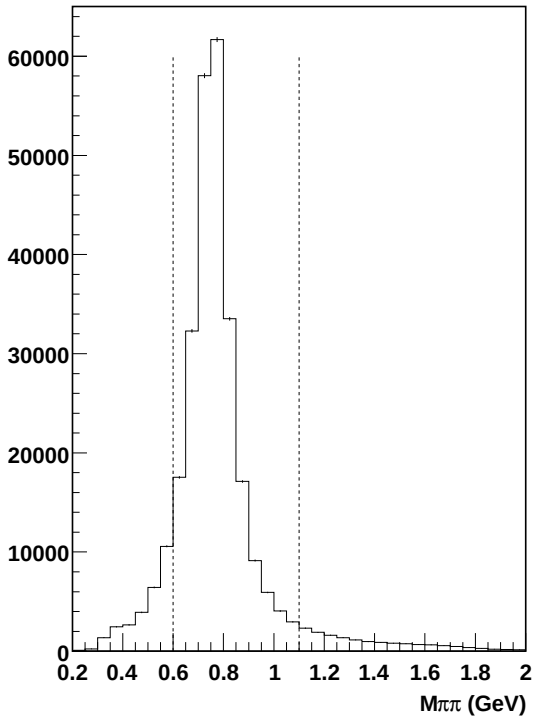

Figure 13: Mass spectrum for selected events shown together with the chosen mass window. The mean value is $< M_{\pi\pi} >= 777.5$ MeV with a RMS value of 192 MeV.

After these cuts, approximately 330 000 events remain. This is the data sample used for the analysis.

4.5 Kinematic region and binning

In section 3.2, the kinematic variables t, W and Q^2 were introduced. Since Q^2 is small in photoproduction, it is not relevant for the event binning and the t and W distributions

determine the kinematic region for the analysis. Figure 20 and 21 show the distributions of t and W respectively for the selected events. As can be seen the t distribution falls exponentially. In order to divide the kinematic region in bins with approximately the same number of events in each bin, a equidistant W-binning with four bins and an non-equidistant t-binning with eight bins is chosen. For the t-binning small bins are used for small t-values and larger bins for larger t-values. In figure 14 the distribution of the selected events in the Wt-plane is plotted together with the binning grid. The bin edges are given by

- $|t|$-binning in GeV^2
  (0, 0.02, 0.05, 0.09, 0.16, 0.30, 0.70, 1.5, > 1.5)

- W-binning in GeV
  (25, 35, 45, 55, 65)

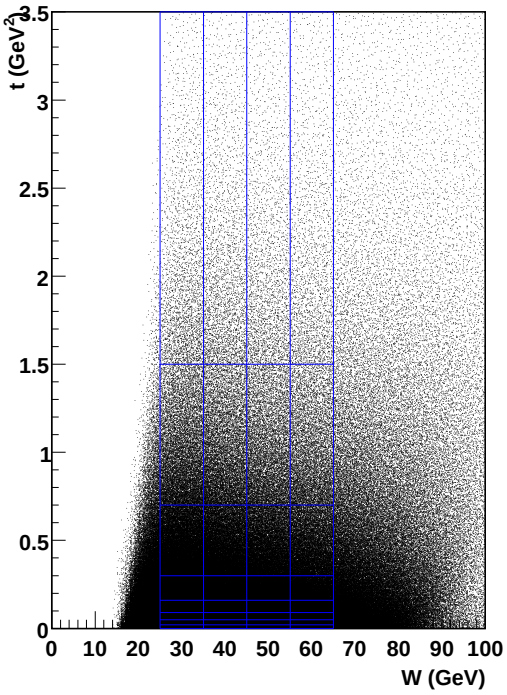

Figure 14: Selected events plotted in the Wt-plane together with the binning used in the analysis.

For distributions measured differentially in W and t, not all 32 bins are presented in this thesis. Instead either one selected Wt-bin or a combination of nine bins (corresponding to three t-bins (low-, medium- and high-t region) and three W-bins (low-, medium- and high-W region)) is chosen.

By studying figure 14, one might think that with the binning chosen lots of events are left

out. The acceptance is however too small outside the chosen region to get accurate results. This is described in more detail in section 4.8.1.

4.6 Background

All processes are exposed to a certain amount of background. In the case of diffractive ρ production, some examples of such reactions are

$$\begin{aligned} \omega &\rightarrow \pi^+ + \pi^- + \pi^0 \\ \phi^* &\rightarrow \pi^+ + \pi^- + \pi^0 \\ \rho' &\rightarrow \pi^+ + \pi^- + \pi^0 \end{aligned} \tag{53}$$

These processes can fake ρ production if the neutral particle is not detected. This might be the case if its energy is deposited in a crack of the detector. This contribution is believed to be small but further studies are needed to verify this assumption.

4.6.1 Non ep background

Background may also come from non ep collisions. The two main contributions are

1. Cosmics
   The atmosphere is constantly being opposed to radiation from space. These charged particles may generate air showers and muons created in this process have a long enough lifetime to reach the detector. Events where a muon of this type hits the detector are called cosmics. They are characterized by a single track penetrating the whole detector and, when showering in the detector, depositing a large amount of energy in the calorimeter. In figure 15, a typical cosmic event is pictured with the H1 Event Display.

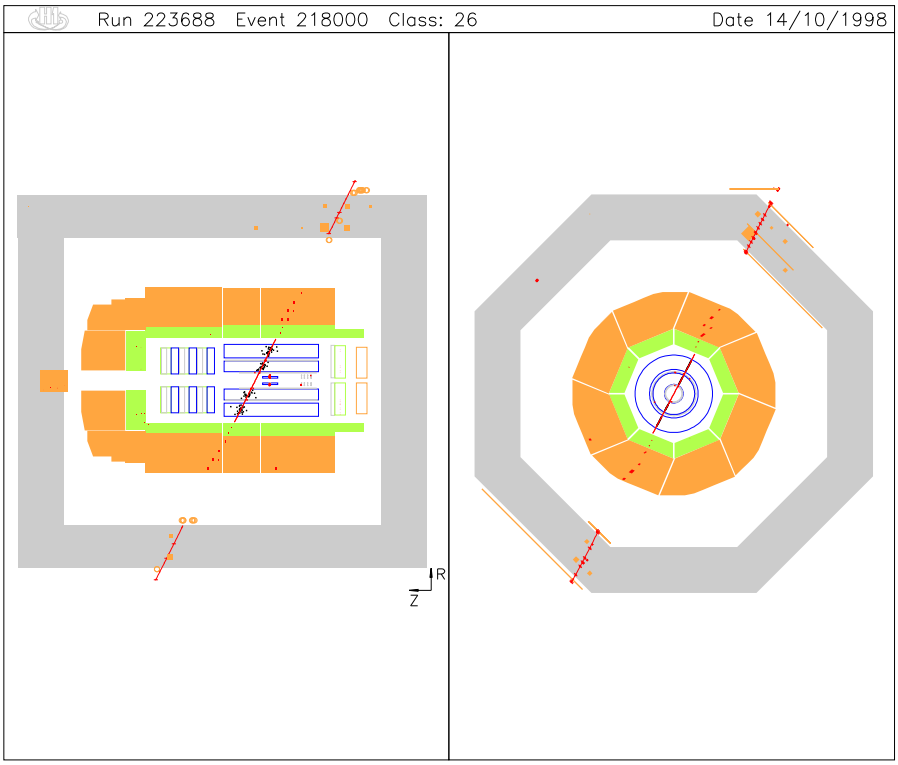

Figure 15: A typical cosmic event with a single track penetrating the whole detector.

It is extermely unlikely that a cosmic event will resemble photoproduction of ρ mesons and *the contribution from the cosmics to the background is therefore negligble.*

2. Beam-gas and beam-wall interactions
   The beam particles can interact with rest gas in the beam pipe or its wall and remnants from these interactions may enter the detector. Timing constraints and vetos (described in the context of Subtrigger 14 in section 4.2.1) surpress the events not originating from the primary interaction point.

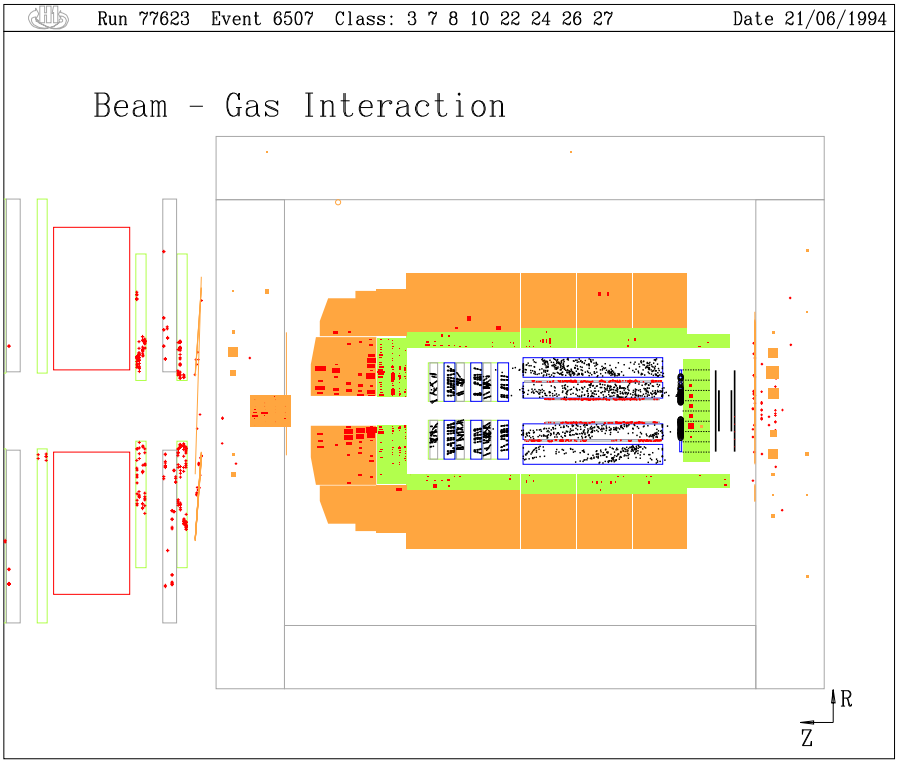

Figure 16: A typical event where the beam particles interact with the beam gas and the walls.

In order to further remove events the vertex cut presented in section 4.4 is applied. This selects a small region around this primary interaction point and a large amount of the beam gas and beam wall events are removed. Taking the vetos and cuts into account *the contribution from beam-gas and beam-wall interactions is very small compared to the photoproduction cross section.*

4.7 Monte Carlo simulation

A central problem in analysing data is to understand the relation between the detector output and the true data. With only the reconstructed data based on the detector output this is an unsolveable problem and is in figure 17 represented by the broken line. The way around this difficulty is to use the software Monte Carlo (MC). As pictured in figure 17 it consists of two parts, first the Monte Carlo generator producing 4-vectors according to the Standard Model and then the Monte Carlo Simulator[7] which simulates the subdetector response of the generated 4-vetors. The result of the detector simulation is finally taken as a input into the reconstruction (H1REC). Since the reconstruction mechanism is the same for MC and data, the input to the reconstruction has to be the same if the output is in agreement. When this is fullfilled, the MC simulation can be used to understand what real values the reconstructed data represent and to correct for unphysical effects.

[7]In this case H1SIM or GEANT

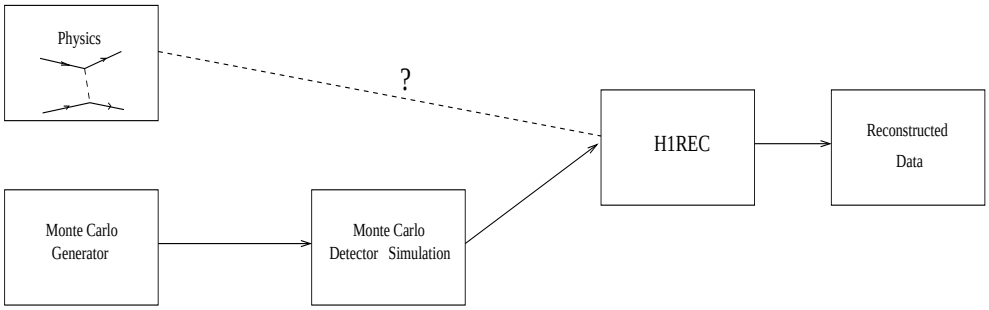

Figure 17: Scheme describing how Monte Carlo simulations can help one understand the detector response and correct the data.

4.7.1 Monte Carlo generator

The Monte Carlo generator used for the analysis is called *Diffvm* and is described in [24]. It simulates diffractive processes in electron-proton scattering within the framework of Regge-phenomology [25, 26, 27] and the Vector Dominance Model (VDM) [28, 29, 30]. In this approach a photon, emitted by the electron, fluctuates into a vector meson which interacts via Pomeron exchange with the proton. Different processes are simulated. The elastic and dissociative processes shown in figure 5 are included and SCHC is assumed in the elastic case. Included in the simulation are also two processes where the photon dissociates, the single diffractive photon dissociation and the double diffractive dissociation (where the photon and the proton both dissociate). All four processes are visualized in figure 18.

The event generation is steered by control cards which are used to fix parameters, for instance

- 4-vectors of colliding particles
- kinematical bounds for the generation of W, y and Q^2
- vector meson type and decay channel

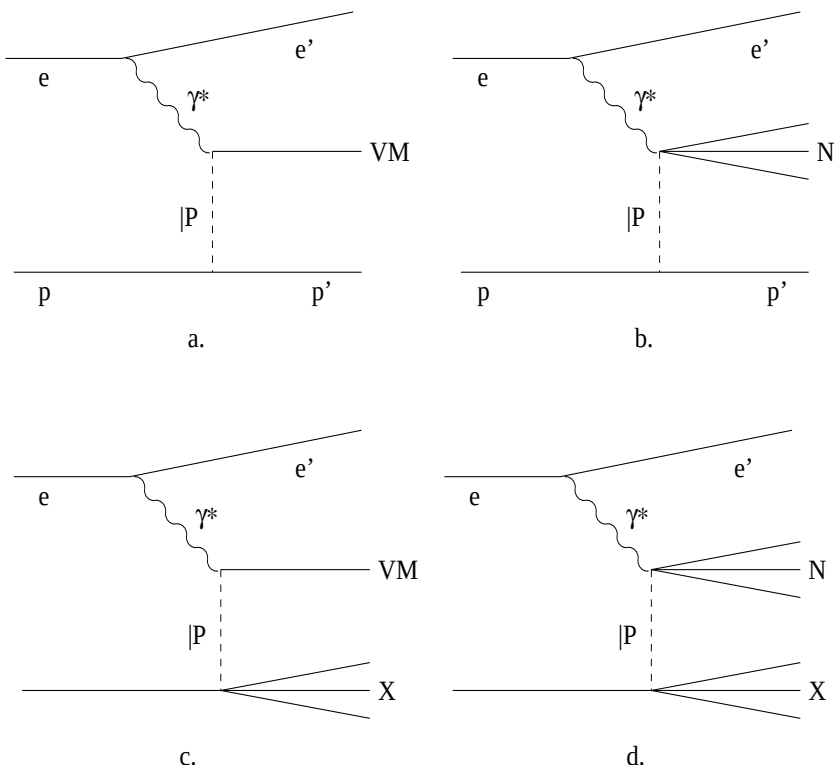

Figure 18: a. elastic phoporoduction, b. single diffractive dissociation of the photon, c. dissociative photoproduction, d. double diffrative dissociation

For the analysis one file with elastic and one with proton dissociative photoproduction are generated. The MC files each contain 10^7 events corresponding to an integrated luminosity of 3928 nb^{-1} for the elastic and 4418 nb^{-1} for the dissociative case.

4.7.2 Control plots

To be able to use the Monte Carlo simulation to correct the data, one has to be sure that the reconstructed values from the simulation well describe the reconstructed data. In figure 19-24 some important kinematic variables are presented. In all figures, the data (black points) is plotted together with the elastic (blue line), the proton dissociative (red line) and the total Monte Carlo production (green line).

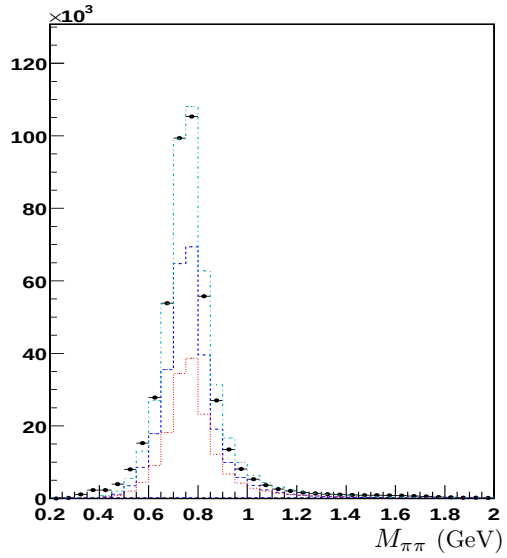

Figure 19: Event distribution of the mass of the ρ candidates.

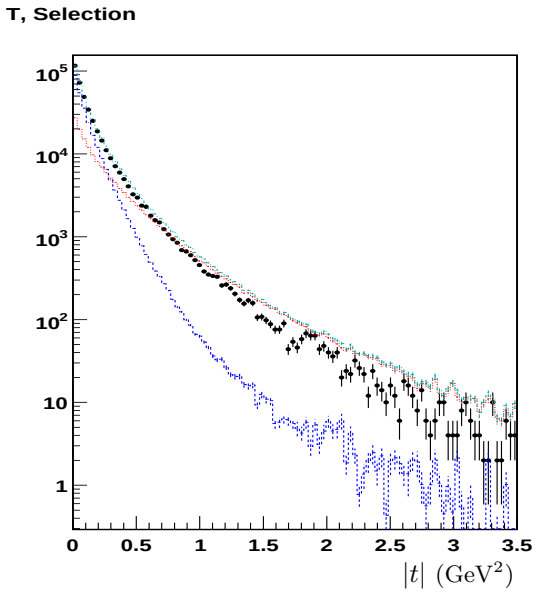

Figure 20: Event distribution of the t-value of the process.

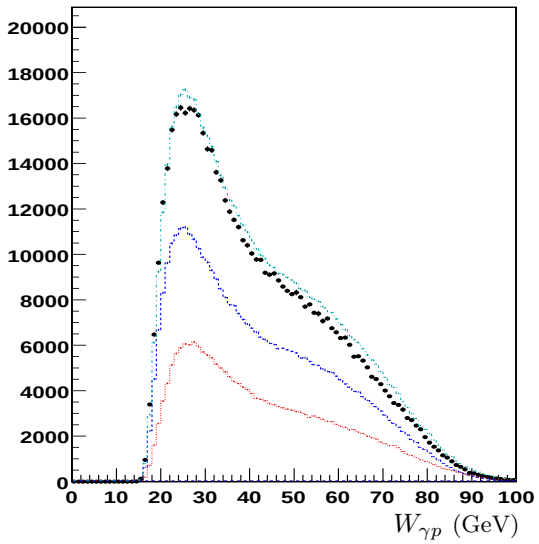

Figure 21: Event distribution of the W-value of the process.

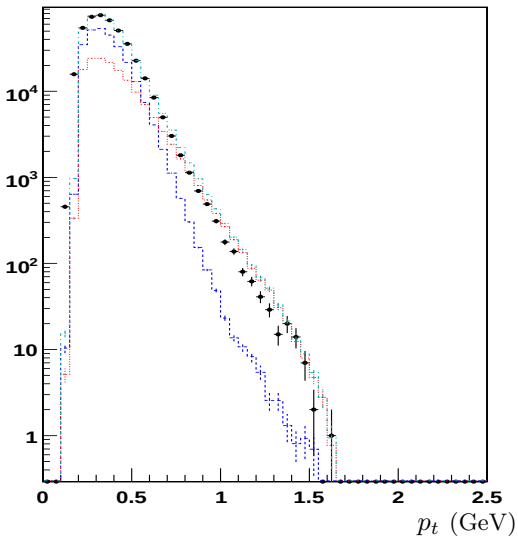

Figure 22: Event distribution of the p_t-value of the pions.

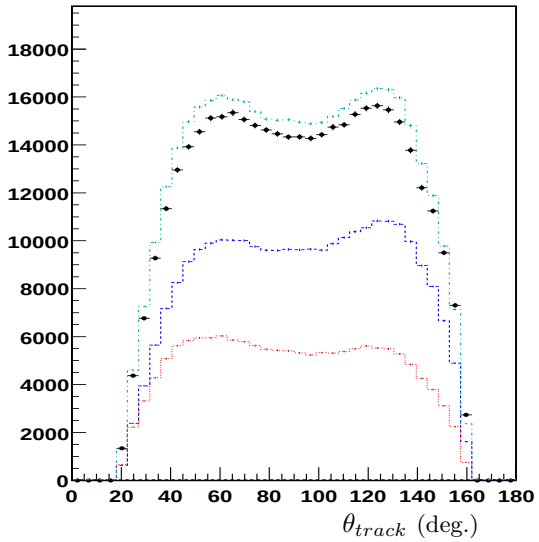

Figure 23: Event distribution of the angle θ between the beam and the track.

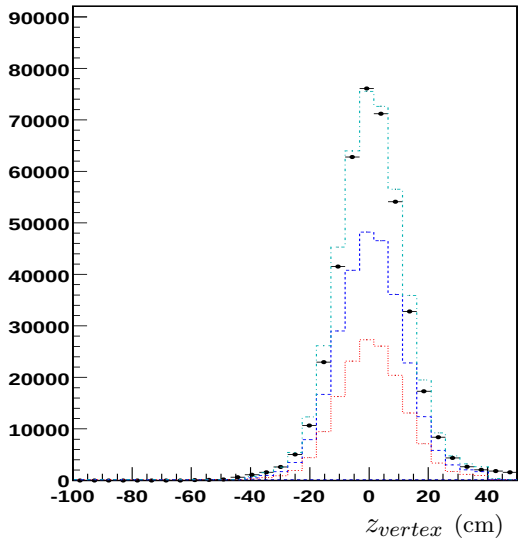

Figure 24: Event distribution of the z-value of the interaction vertex.

As can be seen the Monte Carlo simulation describes the data well and one can use the generated and reconstructed Monte Carlo data to correct the real data. By studying the t-distribution in figure 20 it is also clear why the elastic and proton dissociative processes both are needed. As can be seen they are not equal in t but their sum describes the data well. This is nicely illustrated when studying the low-t region in figure 25.

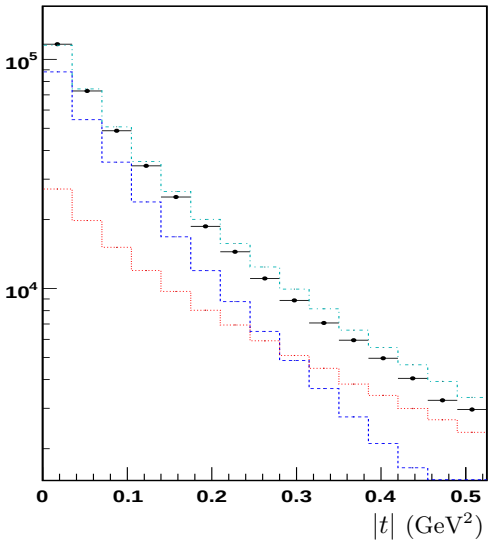

Figure 25: Event distribution in the low-t region.

4.7.3 Reconstruction of helicity angles

In figure 26 a profile plot of $\cos\theta^*_{gen}$ versus $\cos\theta^*_{rec}$ is shown. In such a plot the mean value of $\cos\theta^*_{rec}$ is plotted together with its RMS value for each $\cos\theta^*_{gen}$ bin. In figure 27 the same type of plot is presented for ϕ^*_{gen} versus ϕ^*_{rec}.

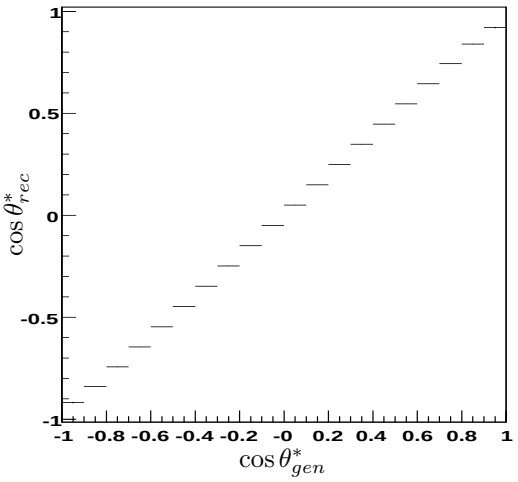

Figure 26: Plot of $\cos\theta^*_{gen}$ vs. $\cos\theta^*_{rec}$.

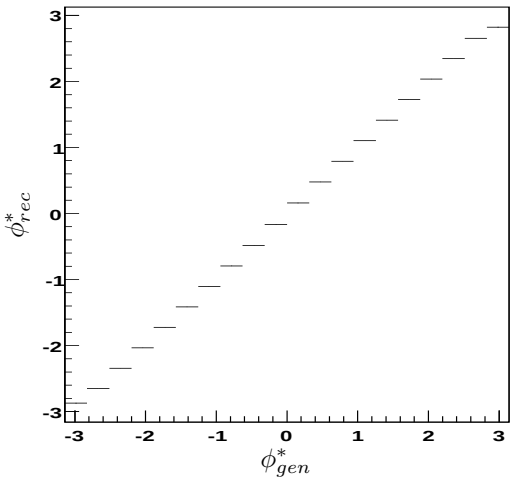

Figure 27: Plot of ϕ^*_{gen} vs. ϕ^*_{rec}.

As can been seen, the reconstructed values describe the generated ones very well. For ϕ^* however, the discrepancy is rather large at the edges. The reason is the ambigious definition

of ϕ^* when the production and decay planes are parallel. Using (7) in section 3.3.2, ϕ^* is calculated according to

$$\phi^* = \arctan\Big(-\frac{\vec{x}\cdot(\vec{z}\times\vec{\pi})}{\vec{y}\cdot(\vec{z}\times\vec{\pi})}\Big) \tag{54}$$

Since the standard C++ function `atan2(x,y)` used to calculate ϕ^* returns a value in the interval $\phi^* \in (-\pi, \pi)$, the problem arises when $\sin\phi^* \to 0$ and $\cos\phi^* \to -1$. Since the angular function is not continious in this region a small change can give rise to a flip from $-\pi$ to π and vice versa. In figure 29, this ambiguity is seen as an abnormal density of events with ${\phi^*}_{gen} = -\pi$, ${\phi^*}_{rec} = \pi$ or ${\phi^*}_{gen} = \pi$, ${\phi^*}_{rec} = -\pi$. Except this detail, the reconstructed values describe the generated ones very well.

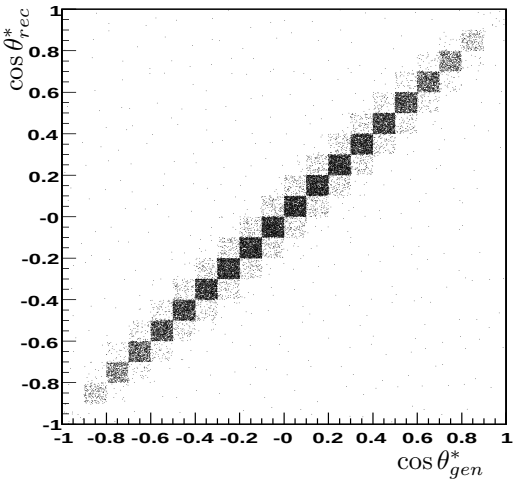

Figure 28: Scatter plot of ${\cos\theta^*}_{gen}$ vs. ${\cos\theta^*}_{rec}$.

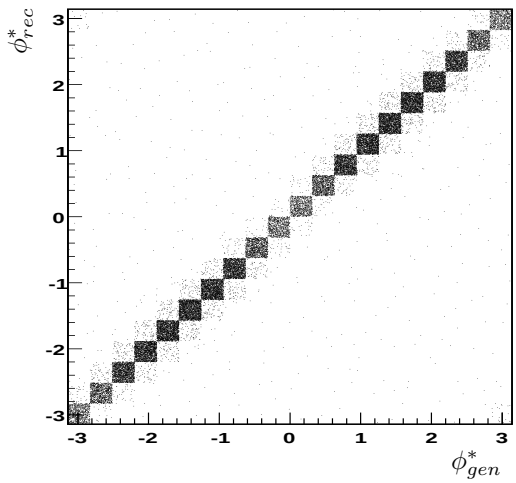

Figure 29: Scatter plot of ${\phi^*}_{gen}$ vs. ${\phi^*}_{rec}$.

4.8 Corrections

As shown in section 4.7.2 and 4.7.3 MC desribes data well and can be used for corrections. The purpose of these corrections is to compensate for effects having impact on the event counting but not displaying the underlying physics. The fact that events where one pion goes down the beam pipe are rejected has for example to be corrected for, since physically, this event is as good as any other in the counting.

In chapter 4.8.1 is step by step described how the Monte Carlo simulation is used to correct the reconstructed data. It should be understood that all the effiencies are functions of W and t and are calculated using the binning given in section 4.5.

4.8.1 Corrections step by step

Below the different steps in the correction procedure are described. For each step the result for $\cos\theta^*$ and ϕ^* for a chosen Wt-bin $\{0.3 < |t| < 0.7 \text{ GeV}^2, \quad 45 < W < 55 \text{ GeV}\}$ is given. The W- and t-variation of the acceptance is presented and discussed in figure **??** in this section. For the efficiencies, the matrices showing the W- and t-variation are given in plots 51-55 in Appendix A.

1. Acceptance, $A = \frac{N_{acc}}{N_{gen}}$

   Not all generated particles are detected and the number of accepted events, denoted N_{acc}, divided by the number of generated events, N_{gen}, directly gives the acceptance. The two main reasons why not all events are detected are geometry (cracks and other detector defects) and kinematic limits (for instance a certain amount of transverse momentum is needed). In figure 30 the acceptance for the chosen Wt-bin is shown.

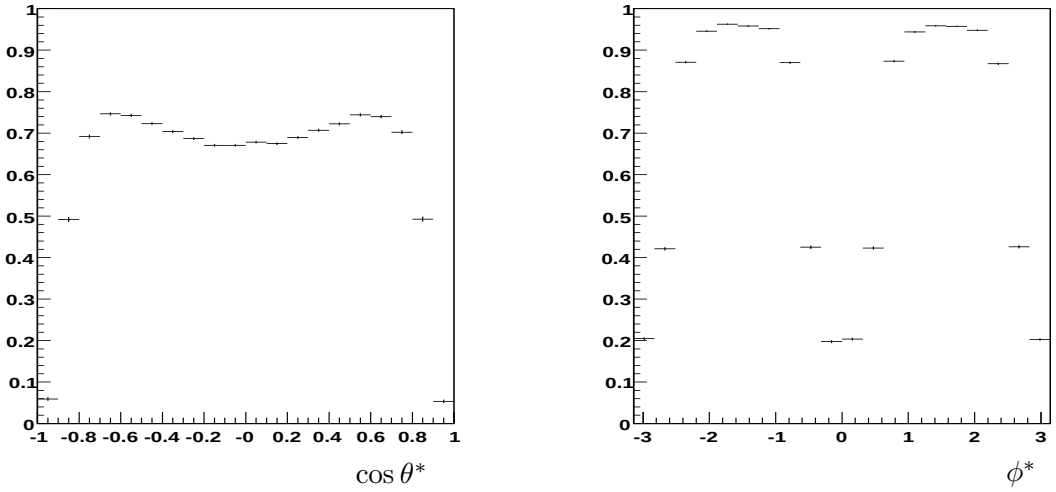

Figure 30: Acceptance for the Wt-bin $\{0.3 < |t| < 0.7 \text{ GeV}^2, \quad 45 < W < 55 \text{ GeV}\}$. To the left for the $\cos\theta^*$ distribution and to the right for ϕ^*.

As can be seen in the right histogram in figure 30, the acceptance varies strongly with ϕ^* and is basically zero when $\phi^* = n \cdot \pi$. The explanation is that for these values of π, the angle between the ρ production and decay plane is small and one of the pions goes down the beam pipe. The demand for two tracks is therefore not fullfilled.
The acceptance also shows a variation with $\cos\theta^*$, as seen in the left histogram in figure 30. The vanishing acceptance in the limit $\cos\theta^* \to \pm 1$ is also due to the demand for two tracks. When $\cos\theta^* = \pm 1$ the polar angle to the positive pion as seen in the rest system of the ρ is 0 or π. In the this system, the two pions are back-to-back and when boosting to the laboratory frame, one of the pions will basically be at rest and will not be able to satisfy the cut on the transverse momentum as stated in section 4.4.

2. Reconstruction efficiency, $\epsilon_{rec} = \frac{N_{rec}}{N_{acc}}$

   Since N_{rec} is calculated from reconstructed variables whereas N_{acc} is calculated from generated variables there is no guarantee that $\epsilon_{rec} < 1$. This is referred to as migration and means that the number of events in a certain kinematic range is overestimated in the reconstruction.

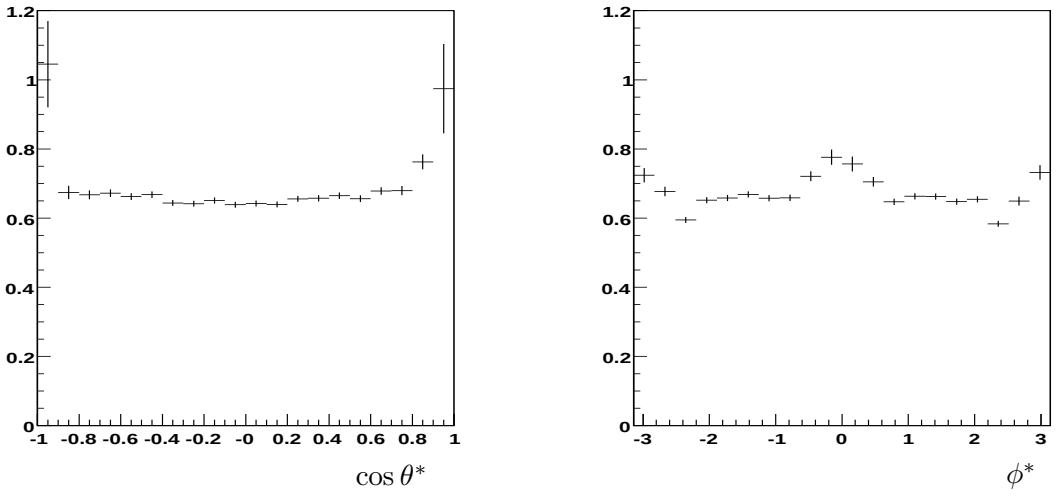

Figure 31: Reconstruction efficiency for the Wt-bin $\{0.3 < |t| < 0.7$ GeV^2, $45 < W < 55$ GeV$\}$. To the left for the $\cos\theta^*$ distribution and to the right for ϕ^*.

   As seen in figure 31, for the reconstruction efficiency one has $\epsilon \approx 0.7$ except for the regions where the acceptance is low. With few accepted events $A \approx 0$ whereas migration of reconstructed events into these regions give $N_{rec} \neq 0$. The end result is then that $\epsilon_{rec} = \frac{N_{rec}}{N_{acc}}$ becomes large.

3. Trigger efficiency, $\epsilon_{trig} = \frac{N_{trig}}{N_{rec}}$

   The trigger efficency is actually the product of a number of trigger efficiencies: the FTT, the CIP and the LAr trigger efficiencies. The a priori expectation is that there is no variation with the helicity angles so that the efficiency is an almost flat distribution. As can be seen in figure 32 this is approximately the case.

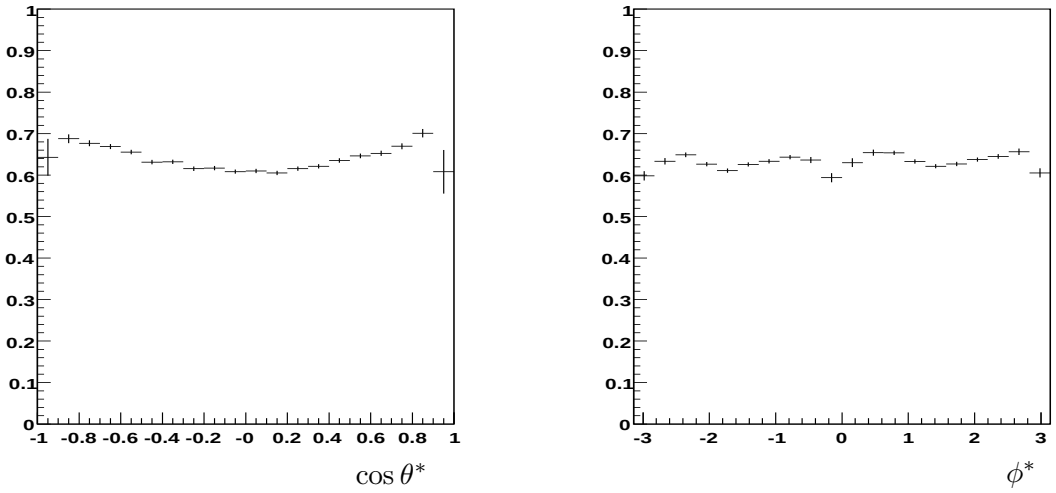

Figure 32: Trigger efficiency for the Wt-bin $\{0.3 < |t| < 0.7$ GeV^2, $45 < W < 55$ GeV$\}$. To the left for the $\cos\theta^*$ distribution and to the right for ϕ^*.

The total efficiency can now be calculated according to

$$\epsilon = A \cdot \epsilon_{rec} \cdot \epsilon_{trig} \stackrel{!}{=} \frac{N_{trig}}{N_{gen}} \tag{55}$$

and this overall efficiency can be used to correct the reconstructed data. An important thing for the analysis is that by using the expression $\frac{N_{trig}}{N_{gen}}$ directly instead of first calculating the different efficiences and then multiply them of course gives the same result but smaller statistical errors.

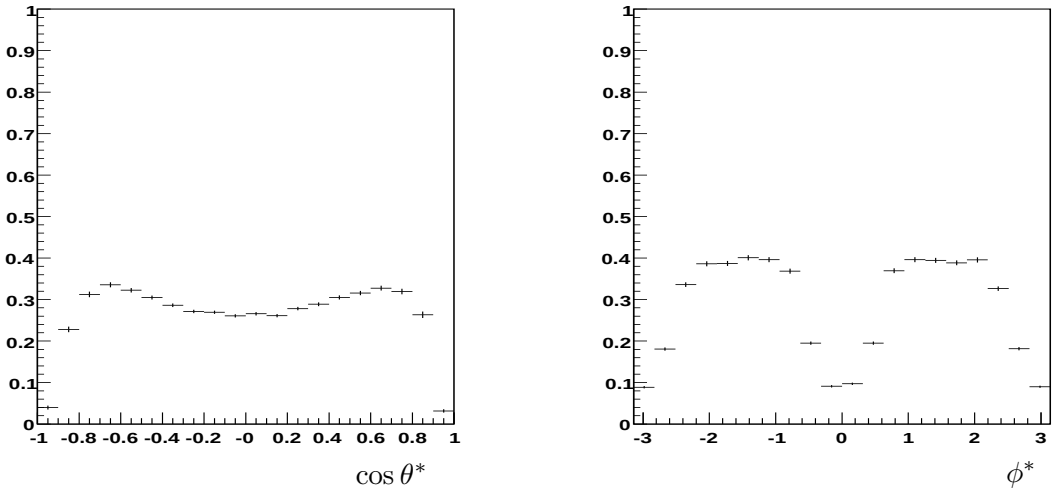

Figure 33: Overall efficiency for the Wt-bin $\{0.3 < |t| < 0.7$ GeV^2, $45 < W < 55$ GeV$\}$. To the left for the $\cos\theta^*$ distribution and to the right for ϕ^*.

The distributions in figure 33 are the ones used to correct the event distribution for the Wt-bin studied here.

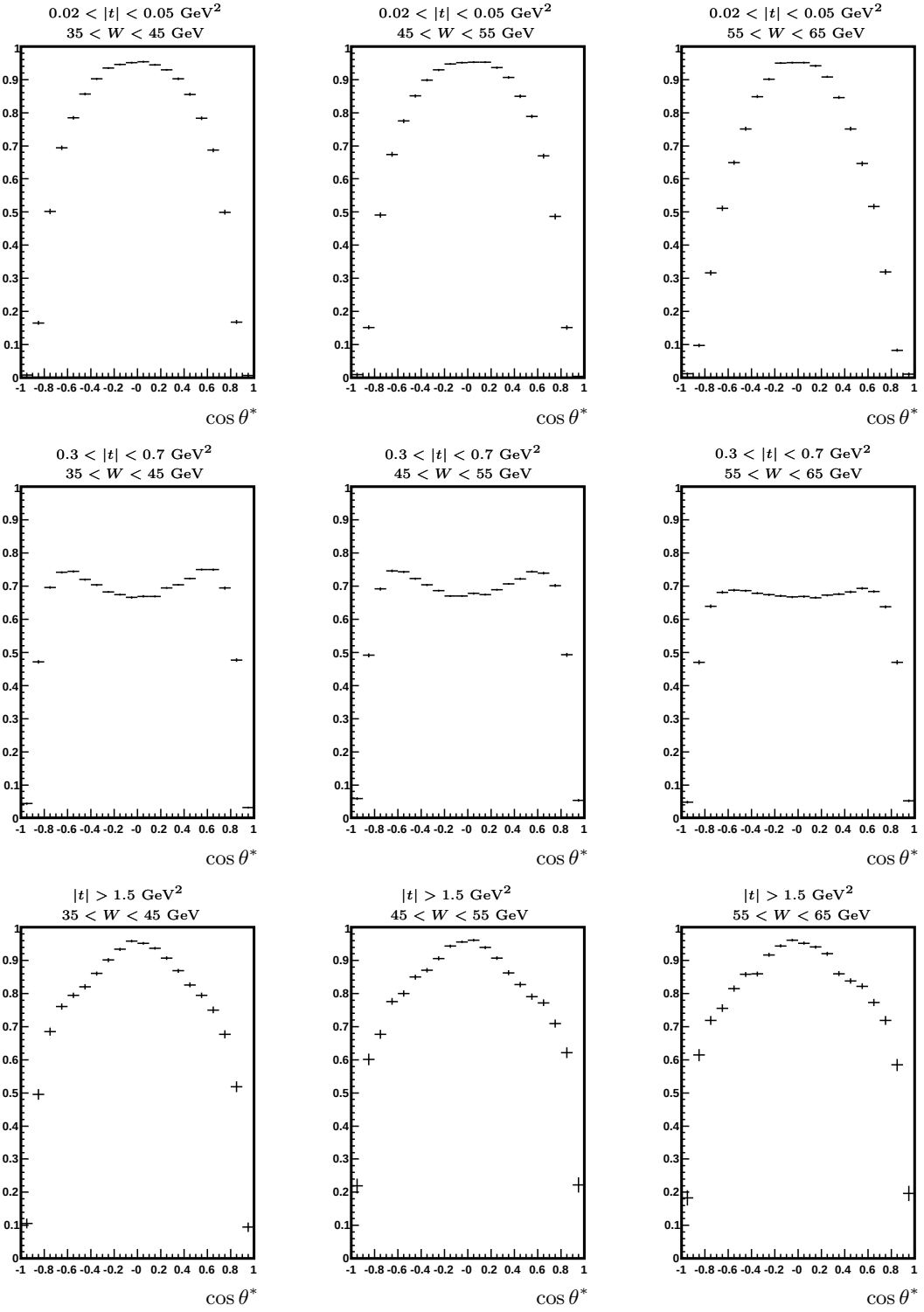

Figure 34: The acceptance as a function of $\cos\theta^*$ plotted for different W- and t-values. W increases from left to right and t when going downwards.

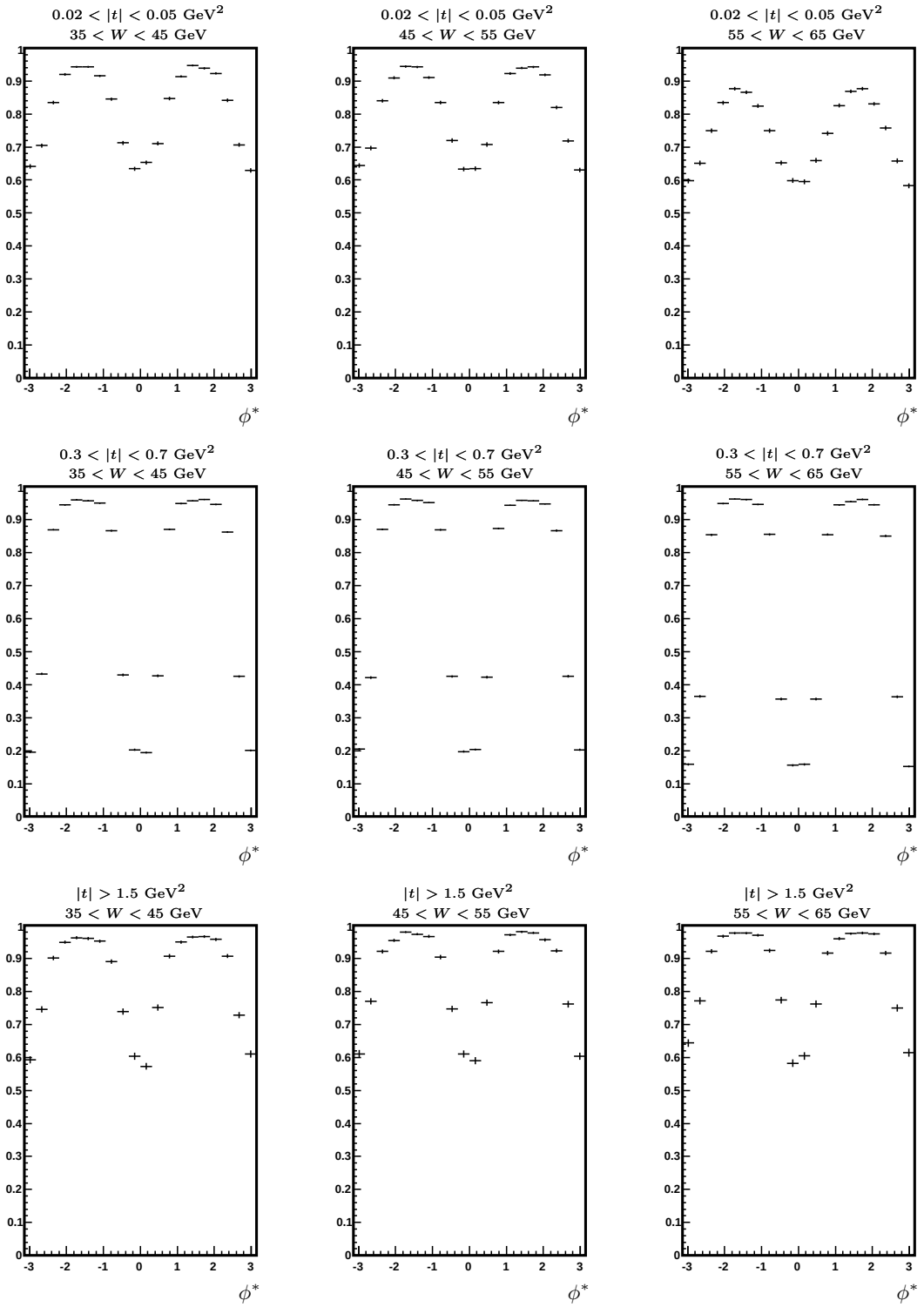

Figure 35: The acceptance as a function of ϕ^* plotted for different W- and t-values. W increases from left to right and t when going downwards.

It is of importance to study how the acceptance varies with the kinematic variables W and t. In figure 34 and 35 one sees that the acceptance is high for small values of $|t|$, decreases appreciably in the region of medium t-values and finally rises again in the high-t region. This behaviour can be understood if the three-vectors of the two pions are studied in the different kinematic regions. The general behaviour is presented in figure 36.

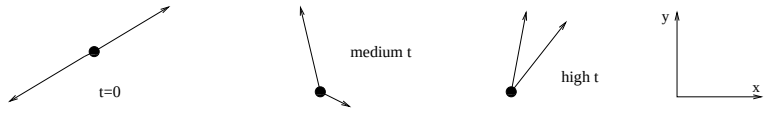

Figure 36: The three vectors of the two pions in different t-regions as seen in the transversal detector plane.

As already mentioned in section 4.4, we demand that each track has a minimum transverse momentum $p_t > 0.2$ GeV. In the region of medium t-values one of the pion vectors really has a small (transverse) momentum and therefore the event does not pass the acceptance cut. Both in the high- and low-t regions, the momentum is more equally distributed between the two pions and therefore more events satisfy the cut.
A similar argument can be used to describe the depletion in the acceptance for small W-values. Figure 37 shows the rz-view of the detector and as can be seen, events with very small and very high W-values have pions vectors making a smaller angle θ_{track} with the beam axis than events with medium W-values. Events with small values of θ_{track} do not pass the selection cut $20^0 < \theta_{track} < 160^0$ given in section 4.4 and this motivates the chosen kinematic range for W as discussed in section 4.5. As seen in figure 34 and 35, the acceptance does not show a large variation with W in the kinematic range $25 < W < 65$ GeV.

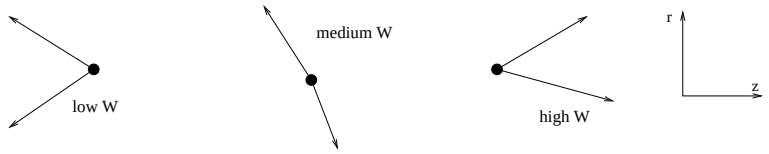

Figure 37: The three vectors of the two pions in different W-regions as seen in the rz-view.

4.9 Fitting

After correcting the angular distributions according to section 4.8.1, a fit to the theoretical curves is performed. Based on equation (9) to (11) the following fitting functions are used

$$f_{\cos\theta^*} = p_3[1 - p_0 + (3p_0 - 1)\cos^2\theta^*] \tag{56}$$

$$f_{\phi^*} = p_3[1 - 2p_1\cos(2\phi^*)] \tag{57}$$

$$f_{2D} = p_3\frac{3}{8\pi}[1 - p_0 + (3p_0 - 1)\cos^2\theta^* - 2\sqrt{2}p_2\sin(2\theta^*)\cos\phi^* - 2p_1\sin^2\theta^*\cos(2\phi^*)] \tag{58}$$

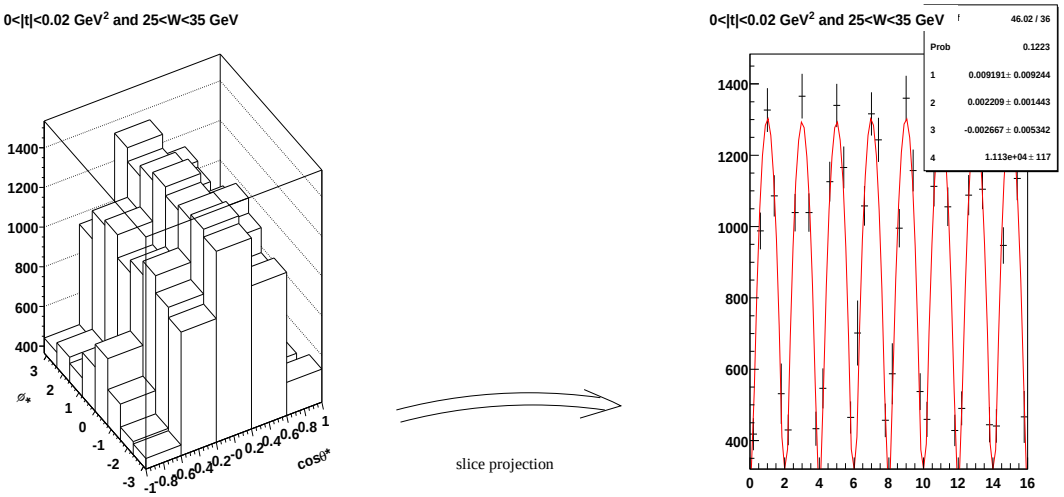

Figure 38: In order to fit a two-dimensional distribution it is first projected as slices onto a one-dimensional histogram.

where p_i describe the fitting parameters. p_0 corresponds to r^{04}_{00}, p_1 to r^{04}_{1-1} and p_2 to $\mathrm{Re}[r^{04}_{10}]$. p_3 is a scale factor not relevant for the helicity properties. A χ^2-fit is used to fit the distributions. Such a fitting routine essentially neglects extremely large or small values associated with large errors.

In this analysis a so called slice projection, seen in figure 38, was made. This means that the two dimensional distribution is cut in slices such that each slice has the same ϕ^*-value. This set of slices, each being a $\cos\theta^*$ distribution for a definite ϕ^*-value is then mapped onto a one dimensional histogram. Since to each value of the one-dimensional histogram, there are definite values of $\cos\theta^*$ and ϕ^*, this histogram can be fitted with (58).

4.9.1 Improved fitting procedure

When fitting a histogram to a given function, the function is evaluated at the bin center. Since one wishes to describe the total number of events in each bin, the fit will be less accurate when the center value is used instead of a weighted mean value. The error associated with the bin-center fitting also increases with increasing bin size. In the two dimensional case, where only five bins for $\cos\theta^*$ and eight bins for ϕ^* are used, this effect cannot be neglected and has to be corrected for. The way this is done is to use the integral of the bin divided by the bin size as a measure of the function value for the fit. If f_{2D} is the original fit function we get

$$f_{2D} = p_3 \frac{3}{8\pi}[1 - p_0 + (3p_0 - 1)\cos^2\theta^* - 2\sqrt{2}p_2 \sin(2\theta^*)\cos\phi^* - 2p_1 \sin^2\theta^* \cos(2\phi^*)] \quad (59)$$

$$F_{2D} = \frac{1}{\Delta_{cos\theta^*}\Delta_{phi}} \int_{\cos\theta^*{}_{min}}^{\cos\theta^*{}_{max}} \int_{\phi^*_{min}}^{\phi^*_{max}} f_{2D} \quad d\cos\theta^* d\phi^* \quad (60)$$

where F_{2D} is the function used for the fitting routine and $\Delta_{cos\theta^*} = \cos\theta^*{}_{max} - \cos\theta^*{}_{min}$ and

$\Delta_{phi} = \phi^*_{max} - \phi^*_{min}$ measure the bin sizes. Carrying out the integration gives

$$\begin{aligned} F_{2D} &= p_3 \frac{3}{8\pi} \frac{1}{\Delta_{cos\theta^*}\Delta_{phi}} [\Delta_{cos\theta^*}\Delta_{phi}(1-p_0) + (3p_0-1)\frac{\Delta_{phi}}{3}({\cos\theta^*}_{max}^{\,3} - {\cos\theta^*}_{min}^{\,3}) + \\ &+ 2\sqrt{2}p_2(\sqrt{1-{\cos\theta^*}_{max}^{\,2}} - \sqrt{1-{\cos\theta^*}_{min}^{\,2}})(\sin\phi^*_{max} - \sin\phi^*_{min}) - \\ &- p_1(\Delta_{cos\theta^*} - \frac{1}{3}({\cos\theta^*}_{max}^{\,3} - {\cos\theta^*}_{min}^{\,3}))(\sin(2\phi^*_{max}) - \sin(2\phi^*_{min}))] \end{aligned} \quad (61)$$

4.10 1D Angular distribution

After applyig the corrections to the one-dimensional event distributions, they are fitted with the functions given in section 4.9. In figure 39 the fitted $\cos\theta^*$ distributions are shown for the matrix consisting of nine different Wt-bins. As can be seen, the shapes are fitted in the range $-0.8 < \cos\theta^* < 0.8$ to avoid the the outermost bins suffering from very large corrections. In figure 40 the fitted ϕ^* distributions are shown for the same matrix of Wt-bins. The ϕ^* distributions are fitted for the full range $-\pi < \phi^* < \pi$.

4.10.1 $\cos\theta^*$ distribution

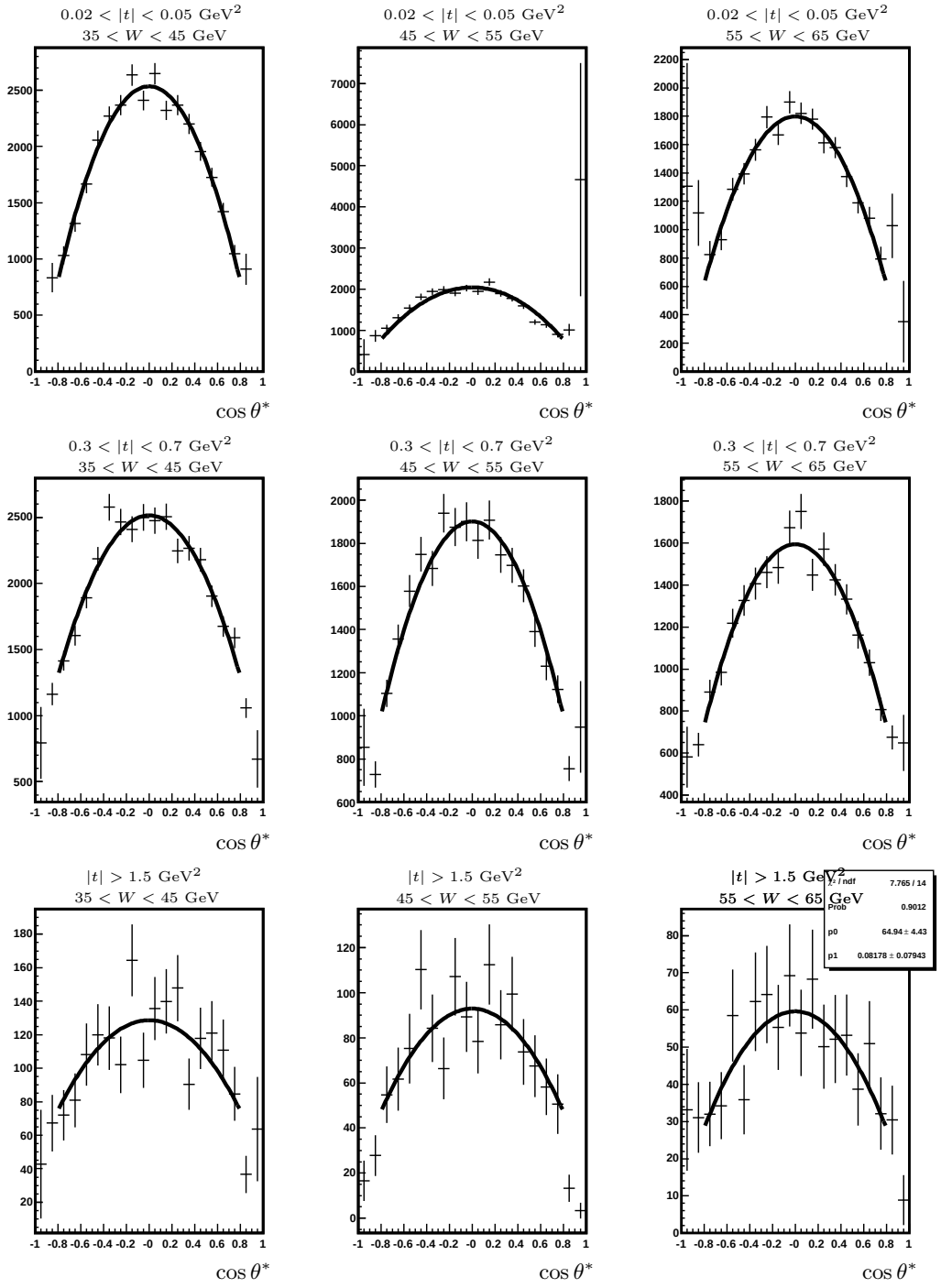

Figure 39: The corrected $\cos\theta^*$ distribution. The y-axis shows the number of events after applied corrections.

4.10.2 ϕ^* distribution

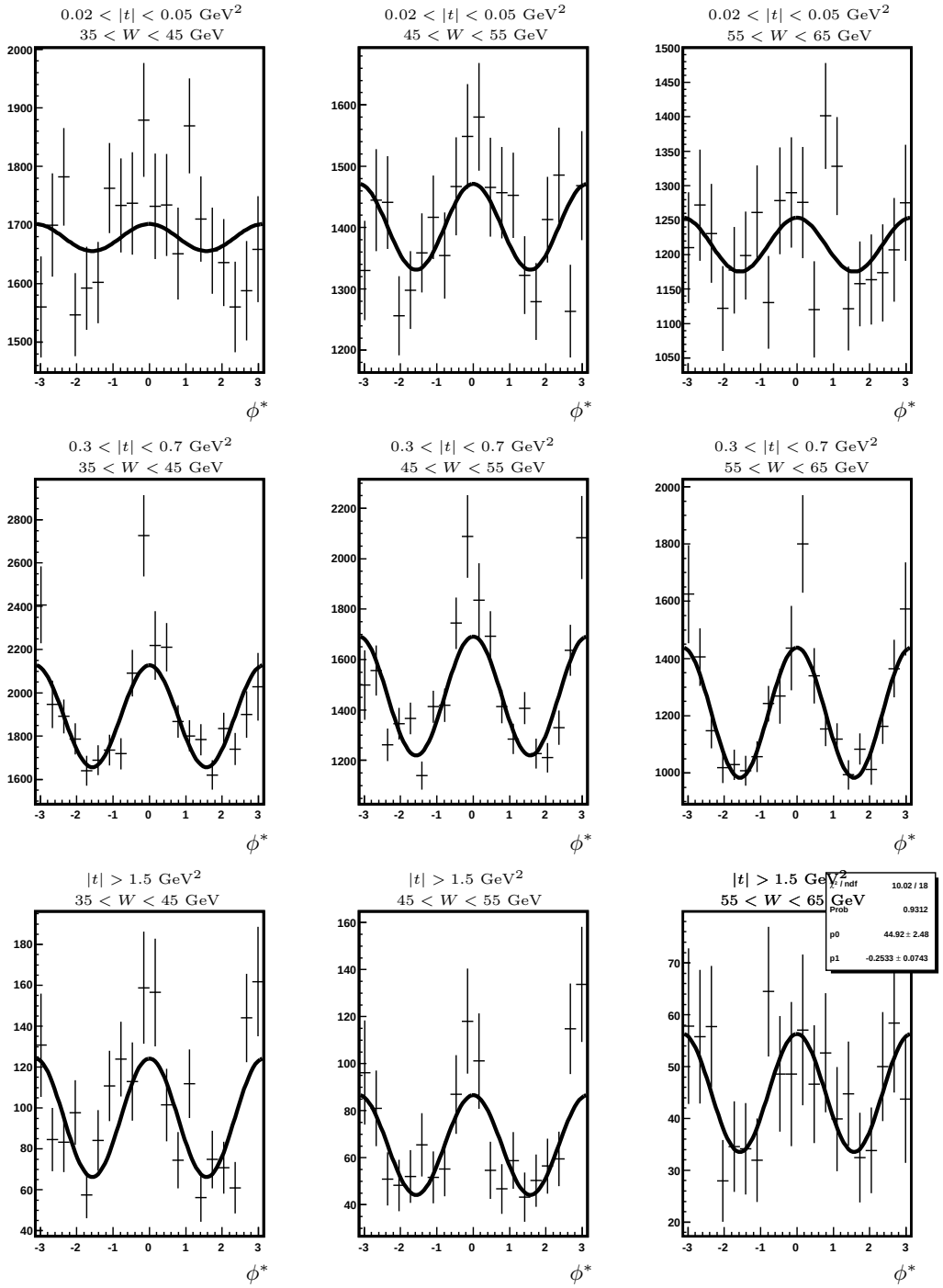

Figure 40: The fitted ϕ^* distribution. The y-axis shows the number of events after applied corrections.

4.11 2D Angular distribution

After correcting the two dimensional event distribution it is slice-projected onto a one dimensional histogram and then fitted with (60). In figure 41 the fitted distributions are presented for the matrix of nine Wt-bins.

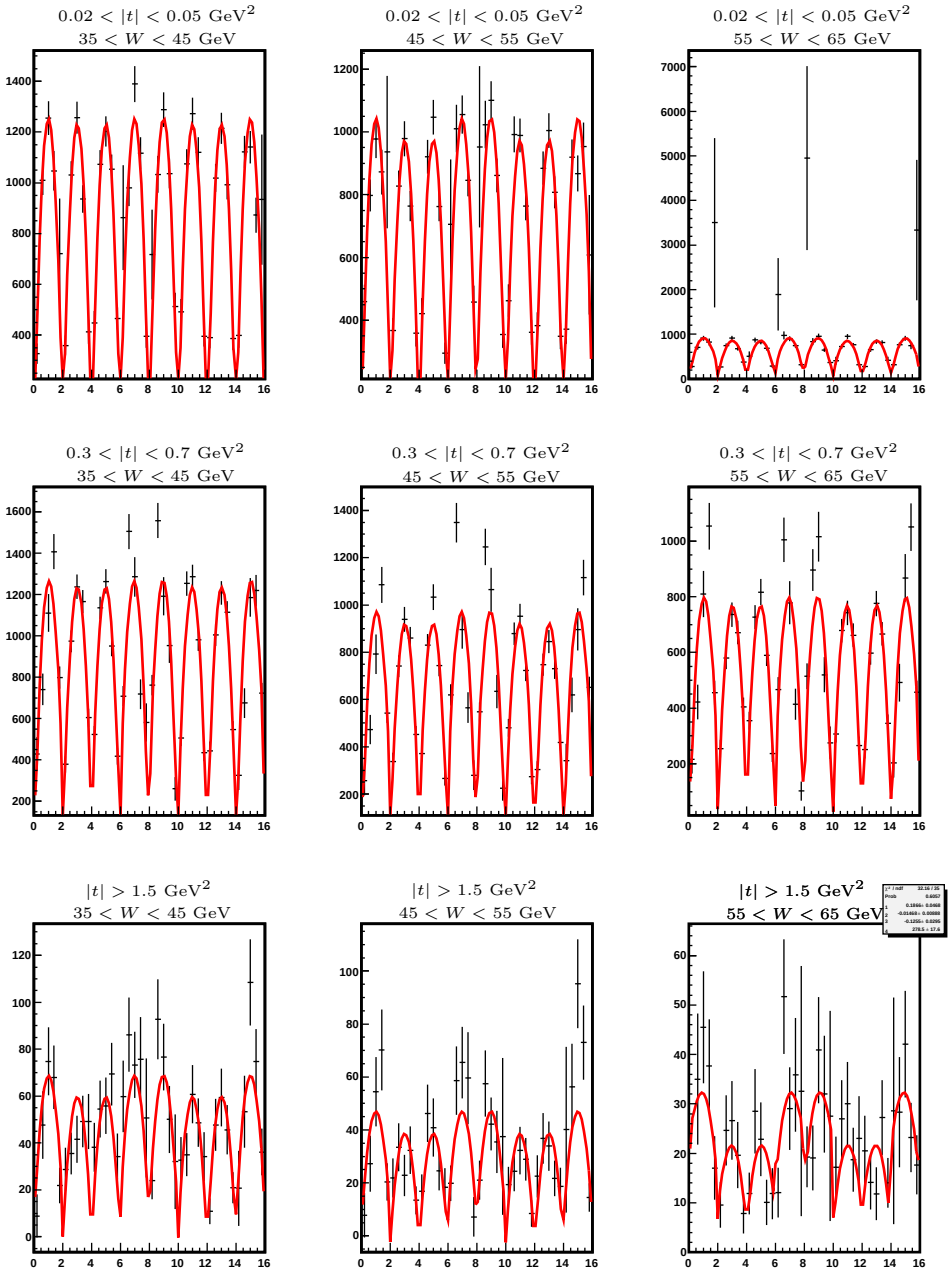

Figure 41: The fitted two-dimensional distribution for the number of events. Here the distribution has first been mapped to an one-dimensional histogram and then fitted. The y-axis shows the number of events after applied corrections.

4.12 Q^2 dependence

As stated before, photoproduction takes place when Q^2 is small. It is also only in the limit $Q^2 \to 0$ that the photon is real and has vanishing longitudinal polarization. A non-zero value of Q^2 therefore means a (small) contribution from the longitudinal polarization of the photon. When analysing the results in this thesis, it is important to realize that this effect can fake SCHNC and that it is only with $Q^2 = 0$ that SCHC implies vanishing spin density matrix elements.

In figure 42 the t-distribution of simulated events, opposed to a Q^2 cut, is pictured. The different curves represent different values on the Q^2 cut. As seen from the distribution of events with $Q^2 > 1.0$ GeV^2, the amount of events is non-negligible. It is also interesting to see that this distribution is not peaked at $t = 0$ like the ones dominated by smaller Q^2-values.

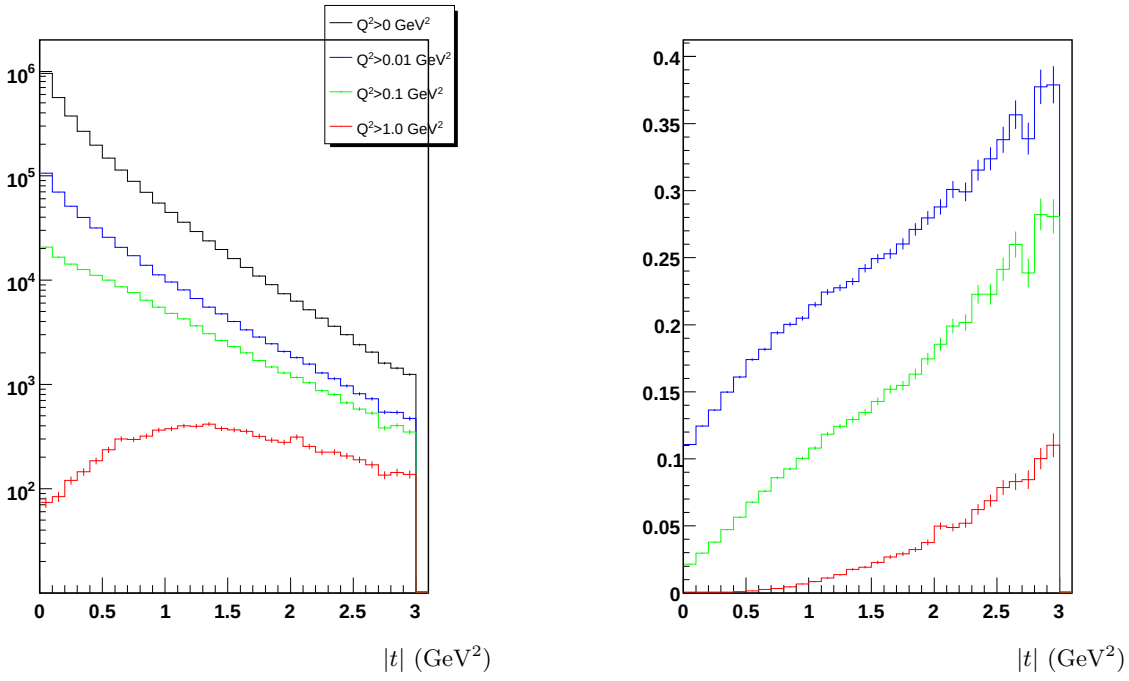

Figure 42: Distribution of selected evens in different Q^2-regions for $0 < |t| < 3$ GeV^2. The black line represents events with $Q^2 > 0$ GeV^2, the blue $Q^2 > 0.01$ GeV^2, the green $Q^2 > 0.1$ GeV^2 and finally the red $Q^2 > 1.0$ GeV^2. The number of events is plotted in the left figure whereas in the right figure each distribution is plotted as fraction of the distribution with $Q^2 > 0$ GeV^2 being normalized to one.

In figure 43, the Q^2 value for the events is investigated in the different t-regions used in the analysis. As can be seen, especially in high-t region, the "contamination" from events with $Q^2 > 1$ GeV^2 is not negliglbe.

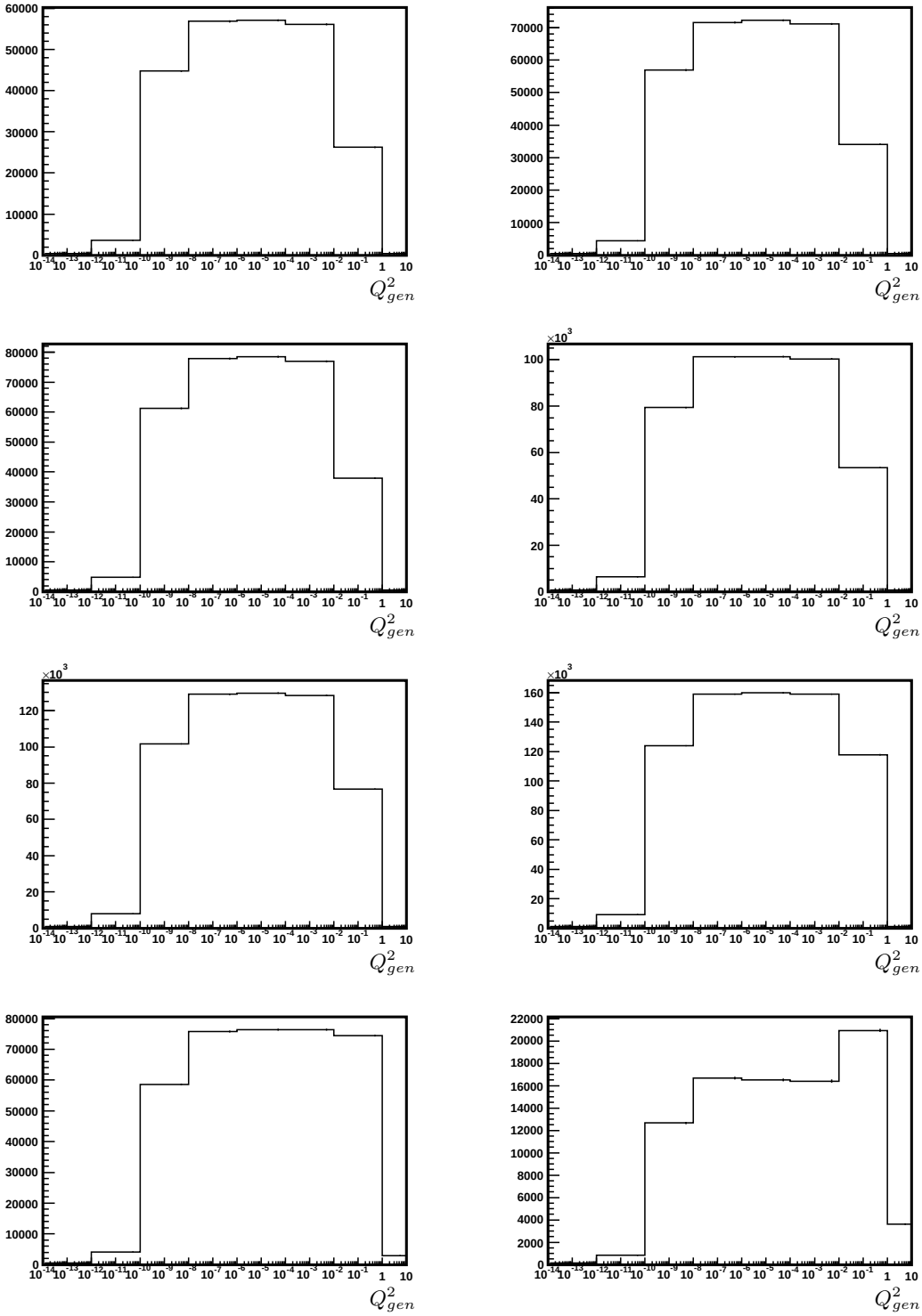

Figure 43: Number of generated events plotted as a function of Q^2 after applied selection cuts. The eight plots represent the eight t-bins used in the analysis, starting with the bin with the lowest t-value in the top left corner and ending with the bin with the highest value in the bottom right corner.

5 Results

In this section, the matrix elements given by the fitted distributions are presented. Each matrix element is graphically presented in section 5.1 to 5.3, first as function of W for the eight different t-values and then as function of t for the four different W-values. The matrix elements r_{00}^{04} and r_{1-1}^{04} can be accesed both from the one- and the two-dimensional distributions and these results are presented together in figure 44-45 (r_{00}^{04}) and 48-49 (r_{1-1}^{04}). The results for all three matrix elements are for each Wt-bin summarized in table 4 to 8 in section B.

5.1 The matrix element r_{00}^{04}

5.1.1 W-dependence

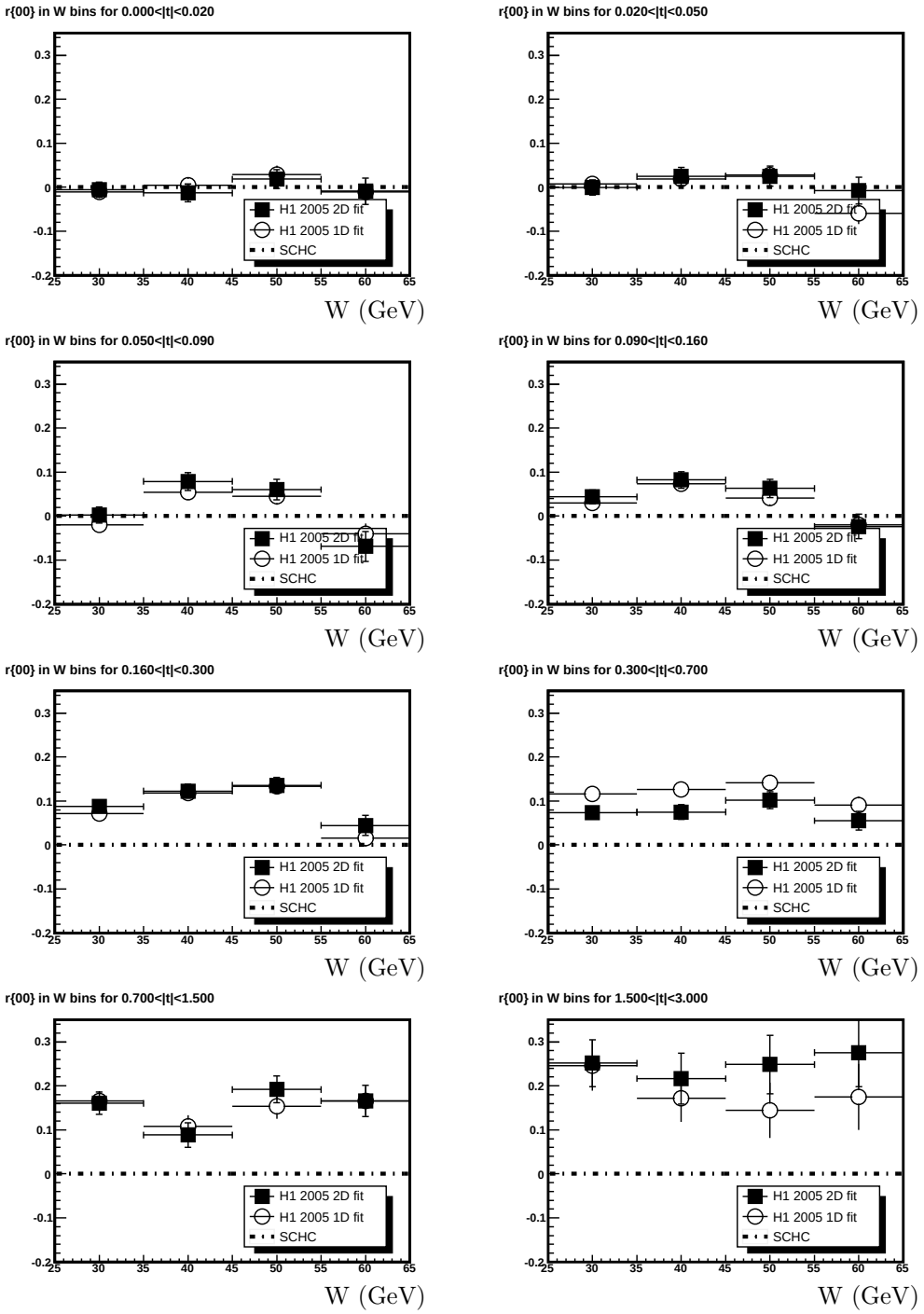

Figure 44: The matrix element r_{00}^{04} plotted as a function of W for different fixed t-values. The white points show the results from fitting the one-dimensional distribution and the black points from fitting the two-dimensional. In the two-dimensional case, the improved fitting routine with $-0.8 < \cos\theta^* < 0.8$ was used.

5.1.2 t-dependence

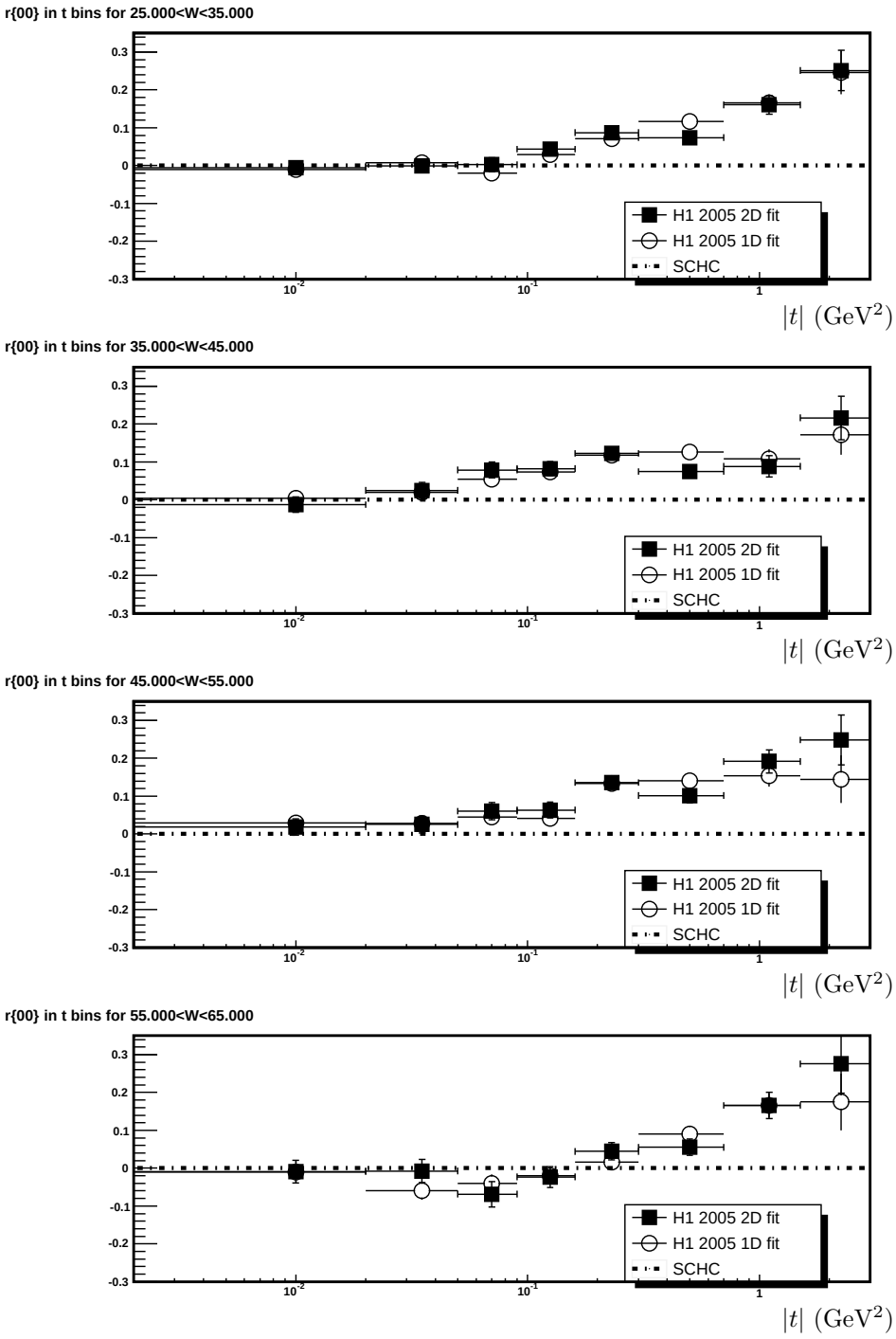

Figure 45: The matrix element r_{00}^{04} plotted as a function of t for different fixed W-values. The white points show the results from fitting the one-dimensional distribution and the black points from fitting the two-dimensional. In the two-dimensional case, the improved fitting routine with $-0.8 < \cos\theta^* < 0.8$ was used.

5.2 The matrix element Re$[r_{10}^{04}]$

5.2.1 W-dependence

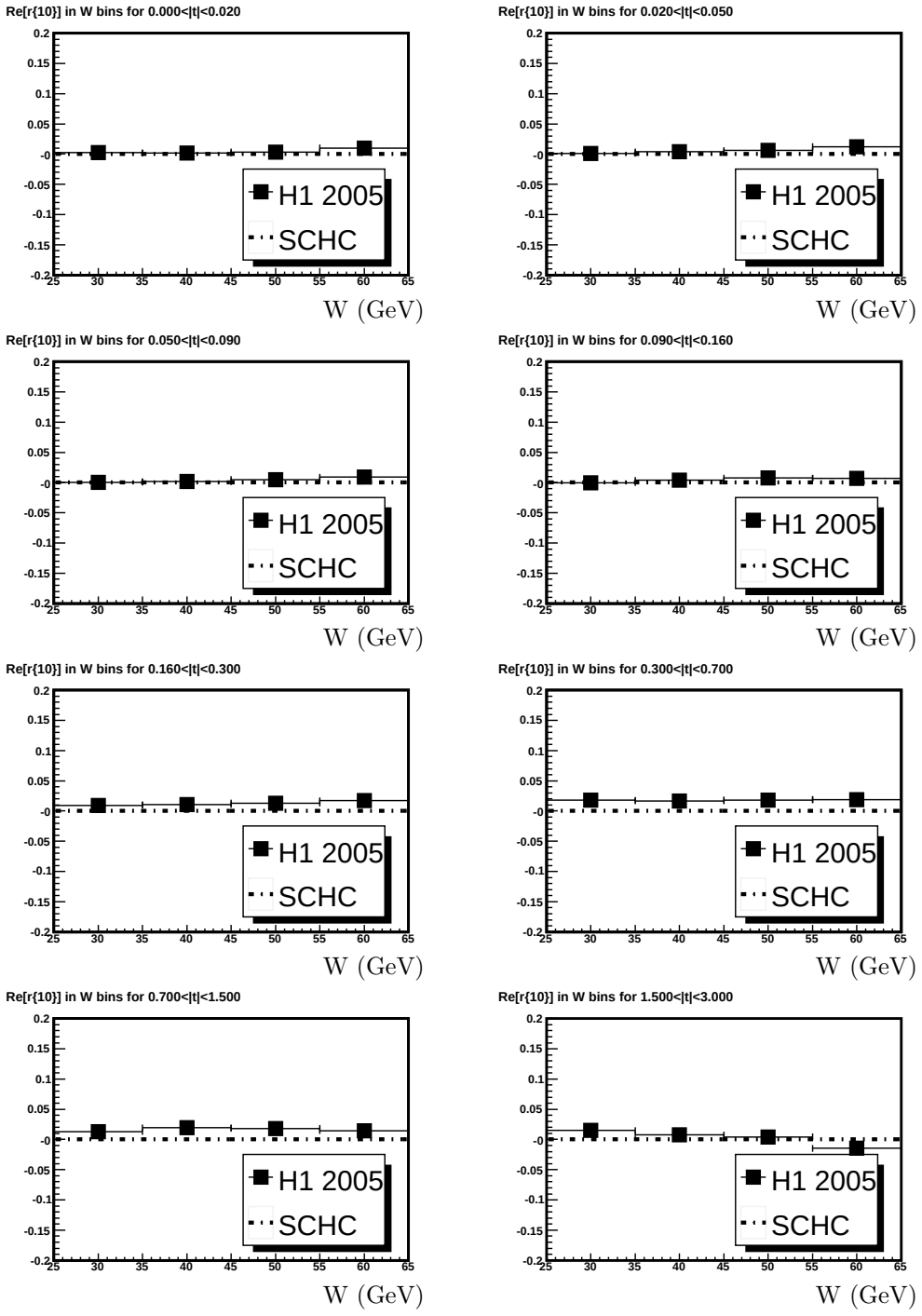

Figure 46: The matrix element Re$[r_{10}^{04}]$ plotted as a function of W for different fixed t-values.

5.2.2 t-dependence

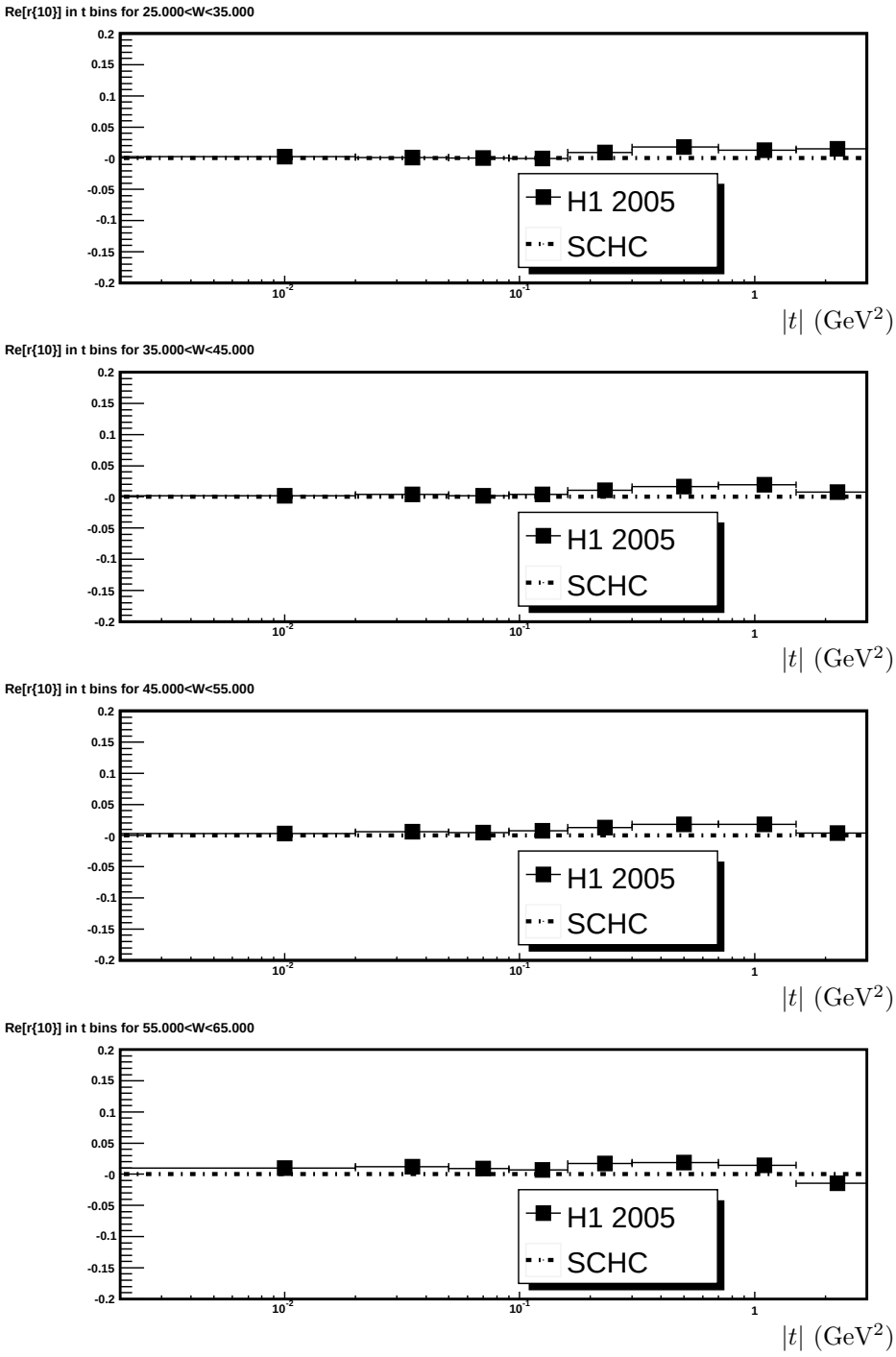

Figure 47: The matrix element $\mathrm{Re}[r_{10}^{04}]$ plotted as a function of t for different fixed W-values.

5.3 The matrix element r^{04}_{1-1}

5.3.1 W-dependence

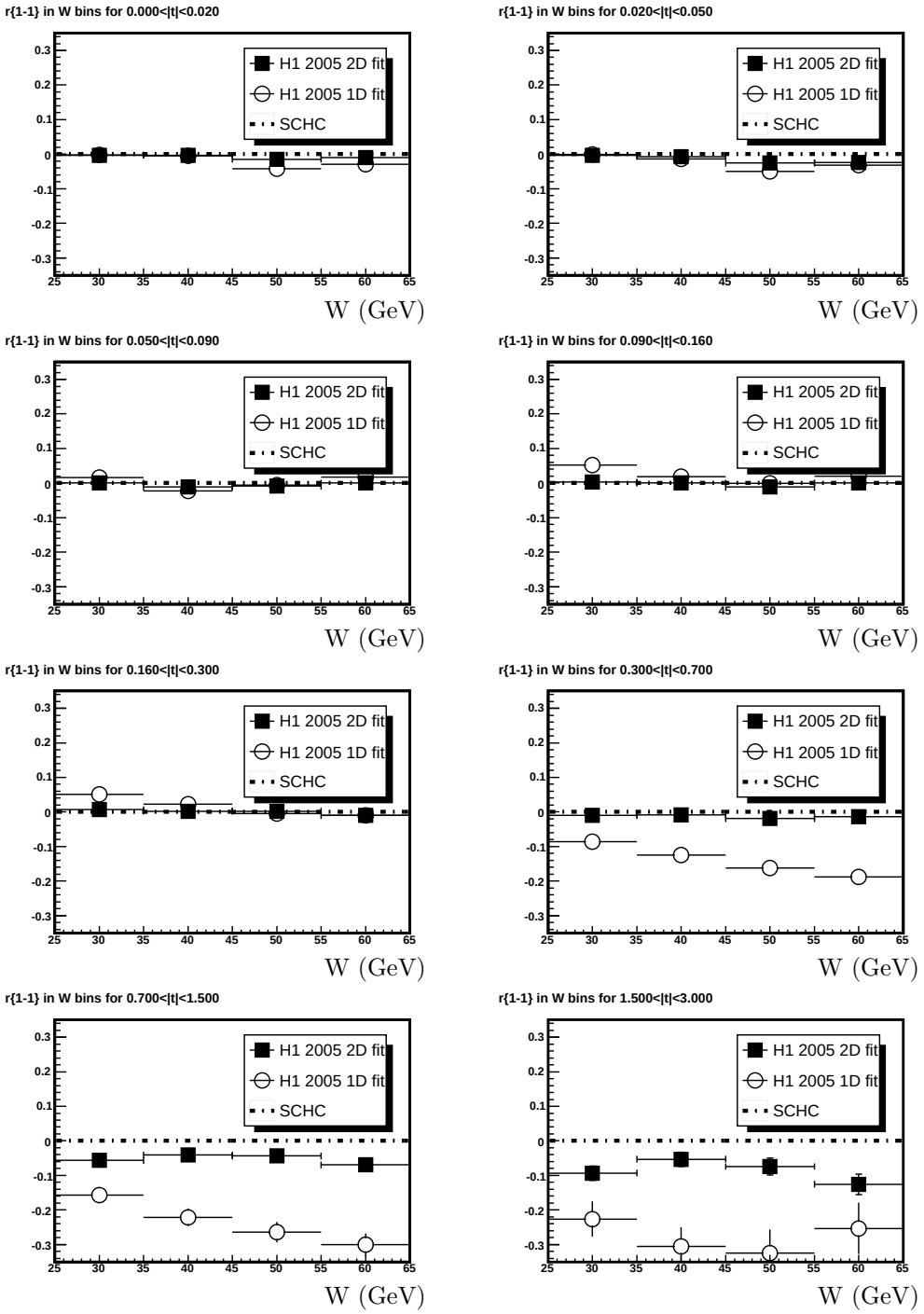

Figure 48: The matrix element r^{04}_{1-1} plotted as a function of W for different fixed t-values. The white points show the results from fitting the one-dimensional distribution and the black points from fitting the two-dimensional.

5.3.2 t-dependence

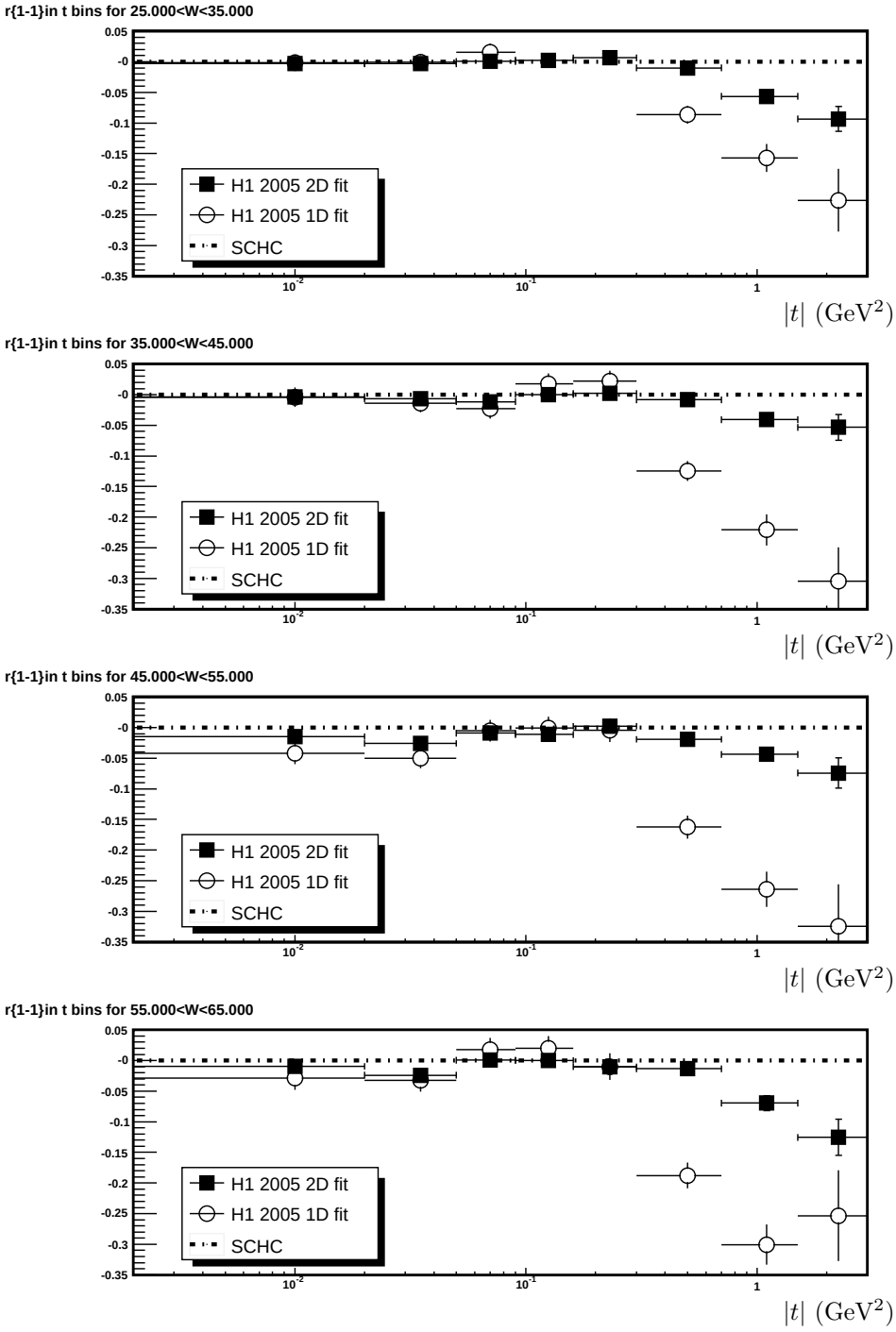

Figure 49: The matrix element r^{04}_{1-1} plotted as a function of t for different fixed W-values. The white points show the results from fitting the one-dimensional distribution and the black points from fitting the two-dimensional.

5.4 Discussion

As seen in figure 44-49 the matrix elements do not show a significant W-dependence. The matrix elements r_{00}^{04} and r_{1-1}^{04} however show a strong t-dependence and are non-zero in the high-t region. $\mathrm{Re}[r_{10}^{04}]$ is for all Wt-bins small and can be considered to be consistent with zero.

It is interesting to compare these results with theoretical predictions and other measurements. The theoretical predictions based on the BFKL model of Poludniowski *et al.* [16, 31] are valid in the region $|t| > 1.0$ GeV^2. In table 2, results for the high-t region extracted from this model are presented for comparison.

$\lvert t\rvert$ GeV^2	r_{00}^{04}	$\mathrm{Re}[r_{10}^{04}]$	r_{1-1}^{04}
1.79	0.012	-0.06	-0.275
2.64	0.022	-0.09	-0.274

Table 2: Predictions based on the BFKL model for the three spin density matrix elements r_{00}^{04}, $\mathrm{Re}[r_{10}^{04}]$ and r_{1-1}^{04}. The values are taken from [6].

In the analysis of C. Gwilliam and X. Jansen [6] the matrix elements r_{00}^{04}, $\mathrm{Re}[r_{10}^{04}]$ and r_{1-1}^{04} were determined in the high-t region ($1.5 < |t| < 10$ GeV^2). The results from their measurement are summarized in table 3.

$\lvert t\rvert$ GeV^2	$<\lvert t\rvert>$ GeV^2	r_{00}^{04}	$\mathrm{Re}[r_{10}^{04}]$	r_{1-1}^{04}
$1.5-2.2$	1.79	$0.038 \pm 0.017^{+0.011}_{-0.012}$	$0.064 \pm 0.012^{+0.006}_{-0.015}$	$-0.088 \pm 0.015^{+0.007}_{-0.014}$
$2.2-3.5$	2.64	$0.029 \pm 0.025^{+0.010}_{-0.013}$	$0.031 \pm 0.019^{+0.007}_{-0.011}$	$-0.138 \pm 0.021^{+0.011}_{-0.011}$
$3.5-10.0$	4.69	$0.062 \pm 0.058^{+0.015}_{-0.012}$	$0.057 \pm 0.034^{+0.004}_{-0.007}$	$-0.119 \pm 0.043^{+0.011}_{-0.009}$

Table 3: Result from the analysis of H1 2000 data [6]. The three spin denisty matrix elements r_{00}^{04}, $\mathrm{Re}[r_{10}^{04}]$ and r_{1-1}^{04} for ρ meson photoproduction are given as a function of $|t|$. The first errors are statistical and the second are systematic. The W-range investigated was $75 < W < 95$ GeV.

If the result from the analysis in [6] is compared with the result for the highest t-bin in this thesis, one sees that the results are in agreement within errors for the values of r_{00}^{04} and r_{1-1}^{04} from the two-dimensional fit. For $\mathrm{Re}[r_{10}^{04}]$ a positive non-zero result is seen in [6] and this contradicts the values seen in this thesis. When comparing the results one should however keep in mind that there are some important differences in the experimental setup. In the year 2000 a so called *electron tagger* was installed (at 44m in the HERA tunnel). This detects the scattered electron at small polar angles in the backward direction. With the electron tagger events with a small photon virtuality ($Q^2 < 0.01$ GeV^2) could be selected and the longitudinal

polarization was, contrary to the analysis in this thesis, negligible. Whereas it is clear that non-zero matrix elements in [6] implies helicity violation it might in this analysis just be a fact of longitudinal photon polarization faking SCHNC. Also the W-values differ in [6]. By using the electron tagger events in the range $75 < W < 95$ GeV were selected. This should be compared with the range $25 < W < 65$ GeV studied in this thesis.

When the results are compared with the BFKL predictions presented in table 2, one sees that for r^{04}_{1-1} the bins with the largest t-value from the one-dimensional fit are in nice agreement with the theoretical model. The results from the two-dimensional fit are however small then the theoretical values. r^{04}_{00} has the correct sign but is larger than the BFKL prediction. For $\mathrm{Re}[r^{04}_{10}]$ the model predicts a small negative value whereas both this analysis gives a result consistent with zero and [6] shows a result of correct magnitude but with positive sign.

The fact that the one- and two-dimensional results for r^{04}_{00} and r^{04}_{1-1} not totally agree is worrying. There are however some differences in the treatment of the two distributions. One thing is the different binnings. In the one-dimensional case 20 bins are used for both $\cos\theta^*$ and ϕ^* whereas eight bins for ϕ^* and five bins for $\cos\theta^*$ are used in the two-dimensional case. More important for the fitting and for the extraction of the matrix elements is however that the outermost bins are totally excluded when fitting the one-dimensional $\cos\theta^*$ distribution. As a first attempt to improve the agreement between the results from the one- and two-dimensional fits, the slice-projection was reconstructed such that only the region $-0.8 < \cos\theta^* < 0.8$ was covered. This improved the agreement for r^{04}_{00} significantly and is shown in figure 44 and 45. For r^{04}_{1-1} no significant improvement was seen and the new fitting routine is not included in figure 48 and 49.

6 Summary and conclusions

In this thesis the helicity properties of diffractively photoproduced ρ mesons were studied using the H1 data taken in 2005. Especially the spin density matrix elements r_{00}^{04}, Re$[r_{10}^{04}]$ and r_{1-1}^{04} were determined as functions of t and W respectively. This was done by studying the decay angular distribution for the ρ meson decaying into $\pi^+\pi^-$. The main result was that the matrix elements r_{00}^{04} and r_{1-1}^{04} have a strong t-dependence and *differ significantly from zero in the region of high t-values*. r_{00}^{04} is positive whereas r_{1-1}^{04} is negative. In the low-t region, both matrix elements are consistent with zero. Re$[r_{10}^{04}]$ is in this analysis showed to be consistent with zero for the whole t-range investigated. The dependence on the kinematic variable W is much weaker and to a good approximation, the matrix elements do not show any W-dependence.

Although the spin density matrix elements r_{00}^{04} and r_{1-1}^{04} are non-zero in the high-t region, it is not clear wheter this is a result of S-Channel Helicity Non-Conservation or just a fact of the non-vanishing longitudinal polarization of the photon. Taking new data using not only the efficient FTT system, but also an electron tagger could be one solution to this problem.

To confirm the resluts in this thesis, further studies have to be made. An improved analysis could be made by considering the following issues

- Understand and correct for the large difference between the values from the one- and two-dimensional distributions. The agreement would be improved if the outermost bins for the two-dimensional distribution were excluded from the fit as in the one-dimenional case. In orde to perform this, constructing a new slice projection and a new fitting function would be necessary.
- Investigation of the impact of bin size and bin number on the final results. Especially in the high-t region the difference for the results from the fitted one- and two-dimensional distributions is large.
- Improve the fitting routines.
- A detailed investigation of systematics. One could for instance investigate the influence of the mass shape and the mean value $< m_{\pi\pi} >$ used for reweighting.
- Another study of systematic errors would be to investigate the influence of the selected mass window $0.6 < m_{\pi\pi} < 1.1$ GeV.
- Investigation of the angular distribution for ρ'. Since this particle has a different distribution for the angular monentum the connection between the helicity violation and the relative angular momentum of the quarks could be better understood.

7 Acknowledgements

This diploma thesis marks the end of my undergraduate physics studies at Chalmers University of technology and ETH Zürich. It has really been a pleasure to be part of the ETH H1 group and there are many people I would like to thank. First of all I am very grateful to Prof. Ralph Eichler for making this thesis possible and for making me feel so welcome in his research group. A very special thank goes to my tutors Dr. Benno List and Ronald Weber for guiding me through the diploma work and for spending so much time on it. Special thanks also to Dr. Christoph Grab and Niklaus Berger for all their help and motivation, to Marc Del Degan and Petra Häfliger for interesting discussions during lunch and coffee breaks, to the part of the group working in Hamburg for their support, to Rosa Bächli for all the help with the administrative work and to the Berger family for the wonderful arrangement in Interlaken. Finally I want to thank my family for their strong and constant support during the last four and a half years.

List of Figures

References

[1] D.R. Yennie, D.G. Ravenhall and R.N. Wilson, Phys. Rev. **95** (1954) 500.

[2] J.F. Gilman *et al.*, Phys. Lett. **B31** (1970) 387.

[3] J. Ballam *et al.*, Phys. Rev. **D7** (1973) 3150.

[4] ZEUS collaboration, J Breitweg *et al.*, Eur. Phys. J. **C2** (1998) 247.

[5] ZEUS collaboration, J Breitweg *et al.*, Eur. Phys. J. **C14** (2000) 213.

[6] C. Gwilliam, X. Janssen, *Diffractive Photoproduction of ρ Mesons with Large Momentum Transfer at HERA*, Publisher, City, Year.

[7] A. Baird *et al.*, IEEE Trans. Nucl. Sci. **48** (2001) 1276 [hep-ex/0104010].

[8] H1 Collaboration, I. Abt *et al.*, Nucl. Instr. and Meth. **A386** (1997) 310 and 348.

[9] N. Berger, *Development of a z-vertex trigger based on drift chamber signals at H1*, Diploma thesis ETH Zürich, ETHZ-IPP internal report 02-04, 2002.

[10] J.R. Forshaw and M.G. Ryskin, Z. Phys. **C68**, 137 (1995) [hep-ph/9501376].

[11] I.F. Ginzburg and D.Y. Ivanov, Phys. Rev. **D54** (1996) 5523 [hep-ph/9604437].

[12] D.Y. Ivanov, R. Kirschner, A. Schafer and L. Szymanowski, Phys. Lett. **B478** (2000) 101 [Erratum-ibid. B 498 (2001) 295] [hep-ph/0001255].

[13] J.R. Forshaw and G.G. Poludniowski, Eur. Phys. J. **C26** (2003) 411 [arXiv: hep-ph/0107068].

[14] J. Bartels, J.R. Forshaw, H. Lotter and M. Wusthoff, Phys. Lett. **B375**, 301 (1996) 5523 [hep-ph/9601201].

[15] D.Y. Ivanov, Phys. Rev. **D53** (1996) 3564 [hep-ph/9508319].

[16] G.G. Poludniowski, R. Enberg, J.R. Forshaw and L. Motyka, JHEP **0312**, 002 (2003) [hep-ph/0311017].

[17] L. Caneschi (ed.), *Regge theory of low-p(T) hadronic interaction*, North-Holland, 1990.

[18] K. Schilling, P. Seyboth and G. Wolf, Nucl. Phys. **B15** (1970) 397.

[19] I.P. Ivanov, N.N. Nikolaev and A.A. Savin, , [hep-ph/0501034]

[20] G.P. Yost *et al.*, Particle Data Group, Phys. Lett. **B204** (1998) 510.

[21] F. Jacquet, A. Blondel, DESY 79-048 (1979) 377.

[22] P. Söding, Phys. Lett. **19** (1966) 702.

[23] T. Zimmermann, *Measurement of Resonance Decays $X \to K^0_s K^0_s$ at HERA*, Diploma thesis ETH Zürich, 2004.

[24] B. List and A. Mastroberardino, *in Proc. of the Workshop on Monte Carlo Generators for HERA physics*, A.T. Doyle *et al.*, DESY-PROC-1999-02 (1999) 396.

[25] T. Regge, Nuovo Cimento **14** (1959) 951.

[26] T. Regge, Nuovo Cimento **18** (1960) 947.

[27] P.D.B. Collins, *An introduction to Regge theory and high energy physics*, Cambridge (Cambridge University Press) (1977).

[28] J.J. Sakurai, Ann. Phys. (NY), **11** (1960) 1.

[29] M. Gell-Mann and F. Zachariasen, Phys. Rev. **124** (1983) 953.

[30] T.H. Bauer, R.D. Spital, D.R. Yennie and F.M. Pipkin, Rev. Mod. Phys, **50** (1978) 261.

[31] R. Enberg, J.R. Forshaw, L. Motyka and G.G. Poludniowski, JHEP **0309**, 008 (2003) [hep-ph/0306232].

[32] P. Ball and V.M. Braun, Nucl. Phys. **B543** (1999) 201 [hep-ph/9810475].

A Efficiency plots

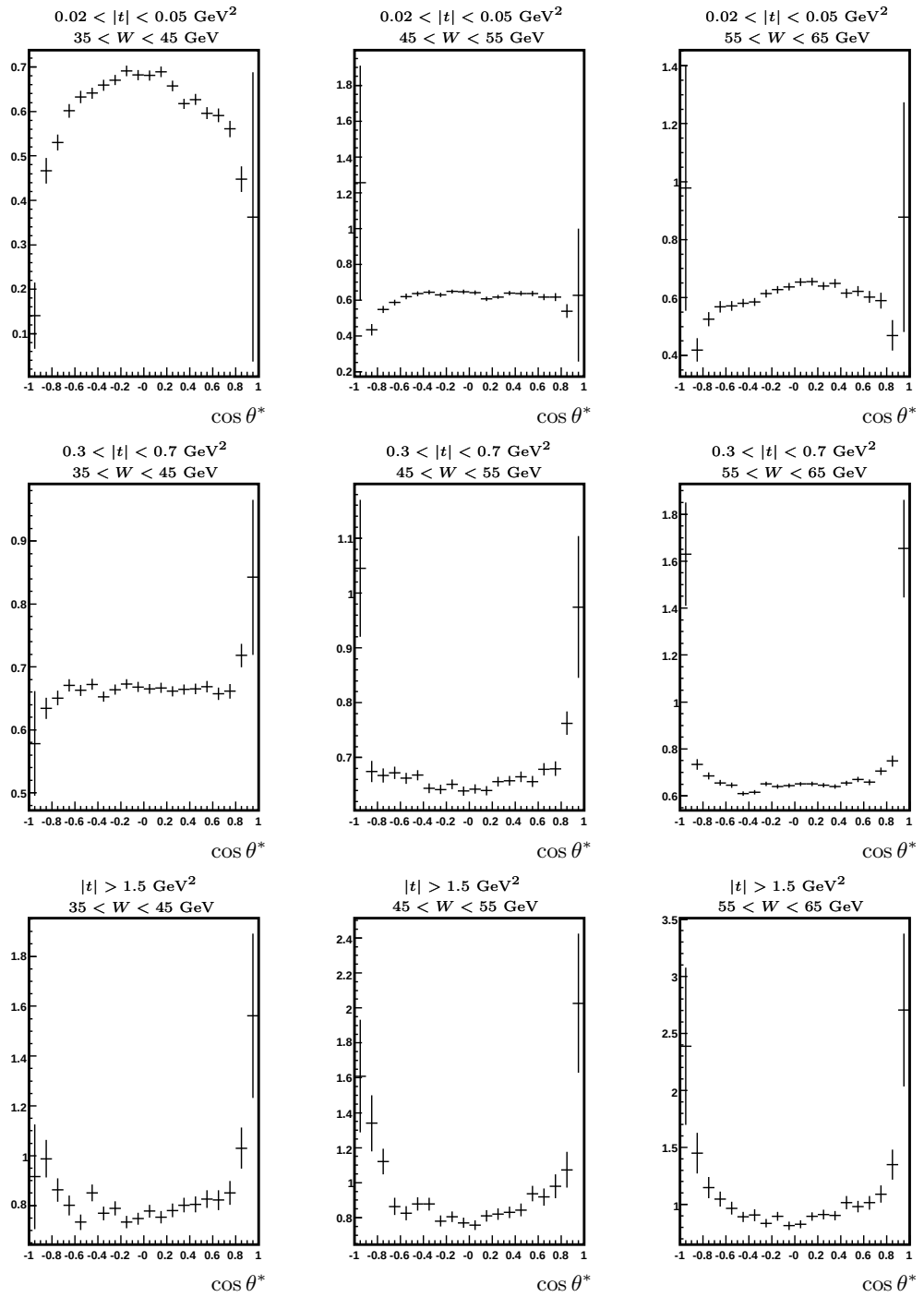

Figure 50: The reconstruction efficiency as a function of $\cos\theta^*$ plotted for different W- and t-values. W increases from left to right and t when going downwards.

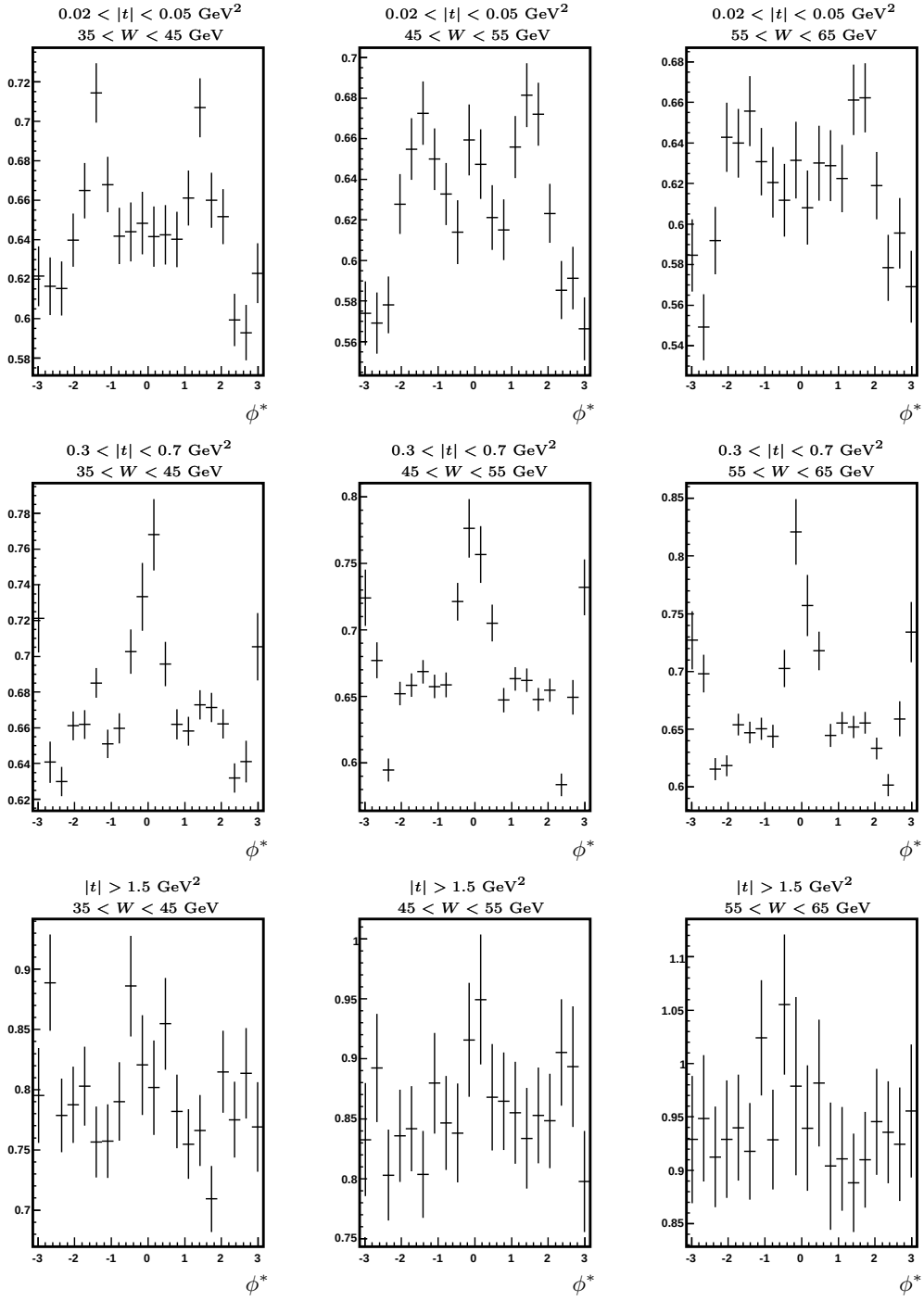

Figure 51: The reconstruction efficiency as a function of ϕ^* plotted for different W- and t-values. W increases from left to right and t when going downwards.

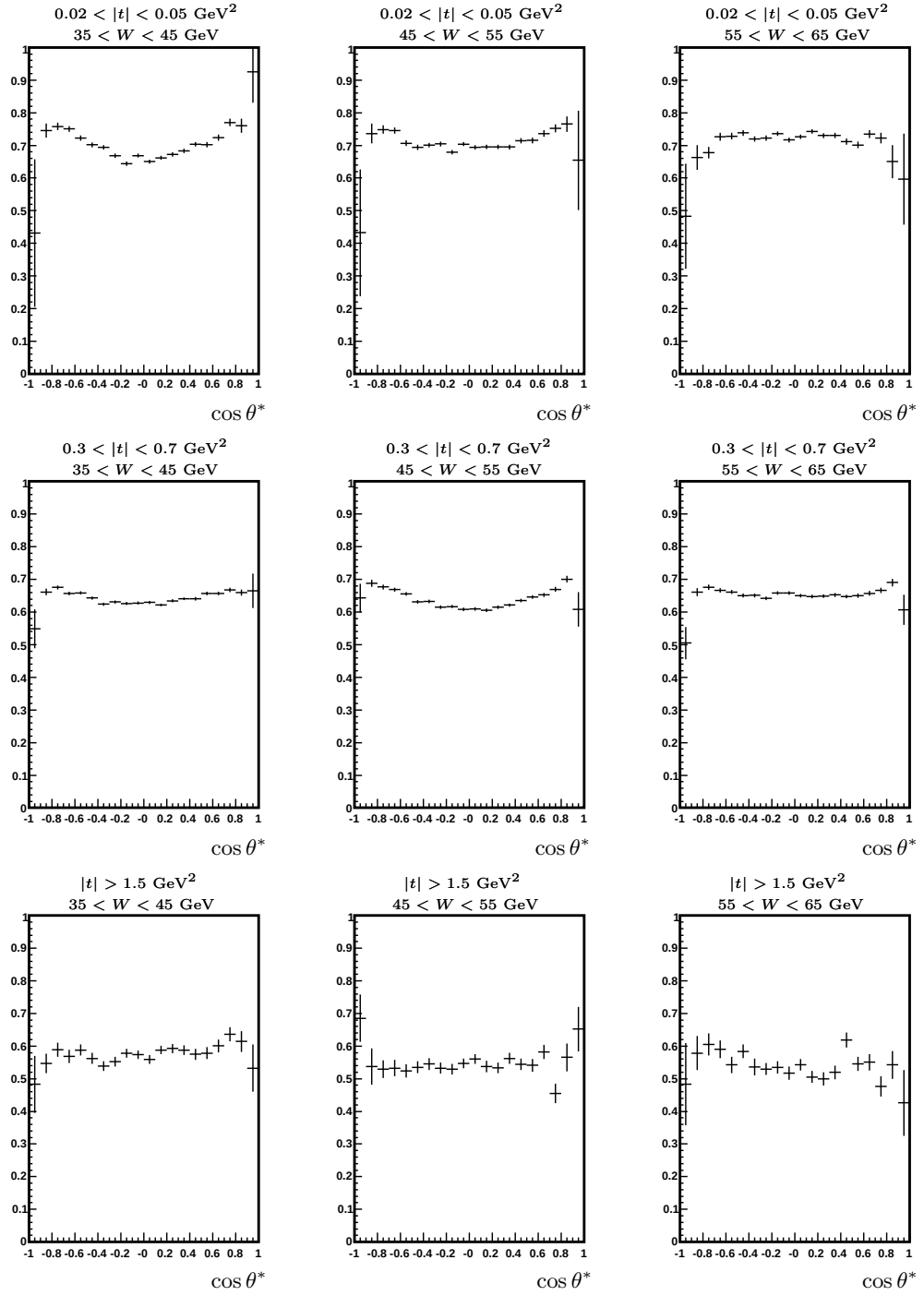

Figure 52: The trigger efficiency as a function of $\cos\theta^*$ plotted for different W- and t-values. W increases from left to right and t when going downwards.

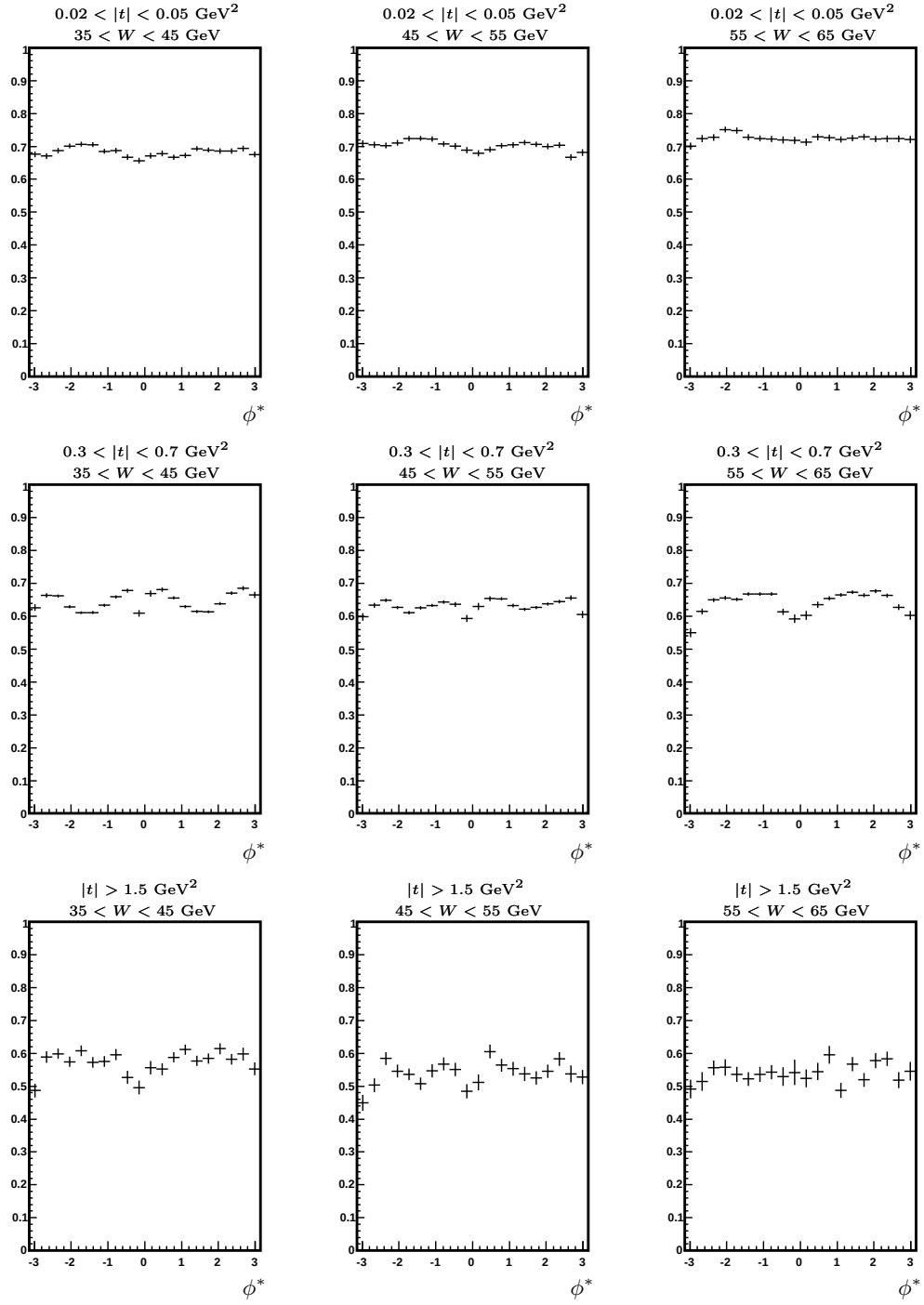

Figure 53: The trigger efficiency as a function of ϕ^* plotted for different W- and t-values. W increases from left to right and t when going downwards.

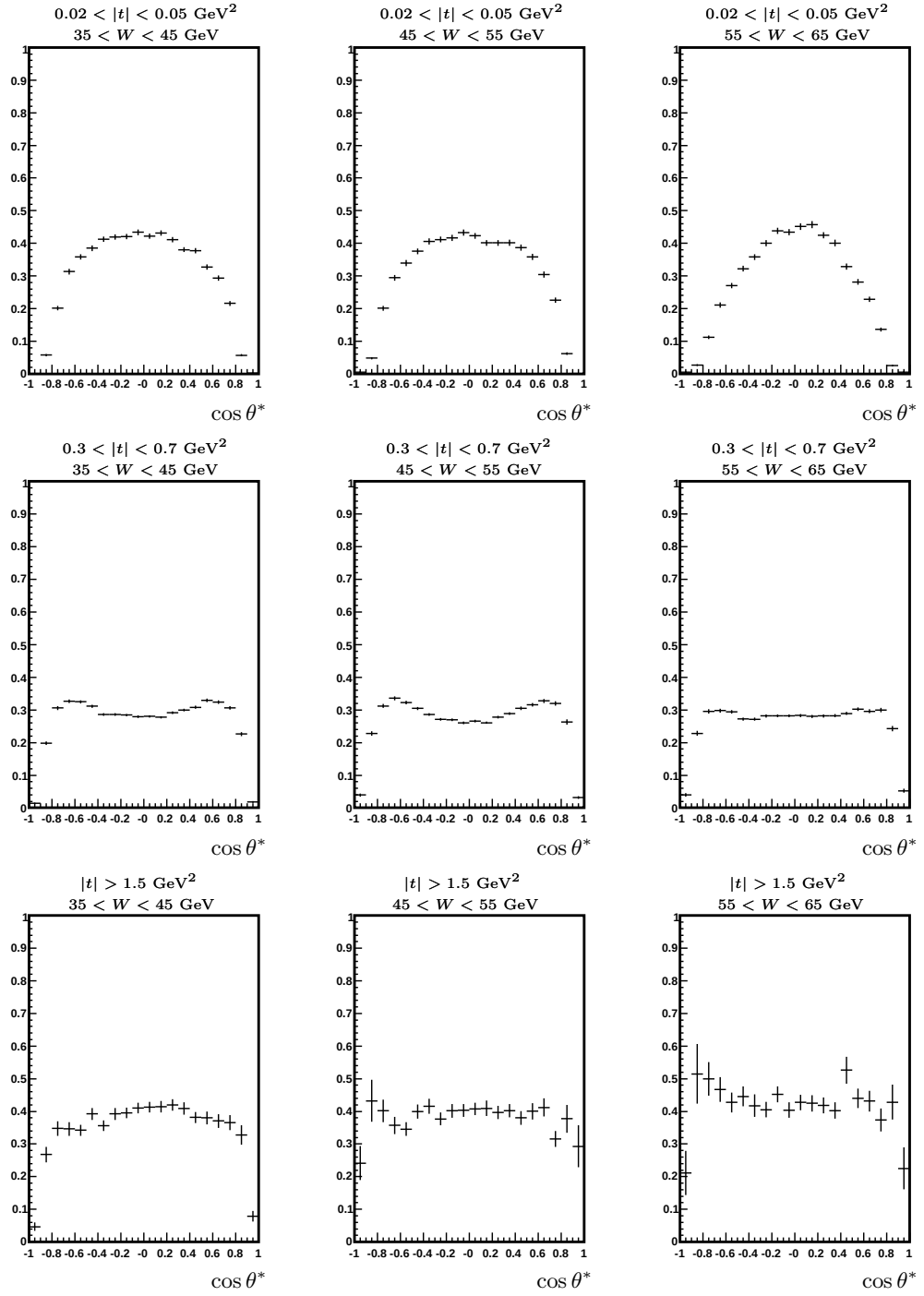

Figure 54: The overall efficiency as a function of $\cos\theta^*$ plotted for different W- and t-values. W increases from left to right and t when going downwards.

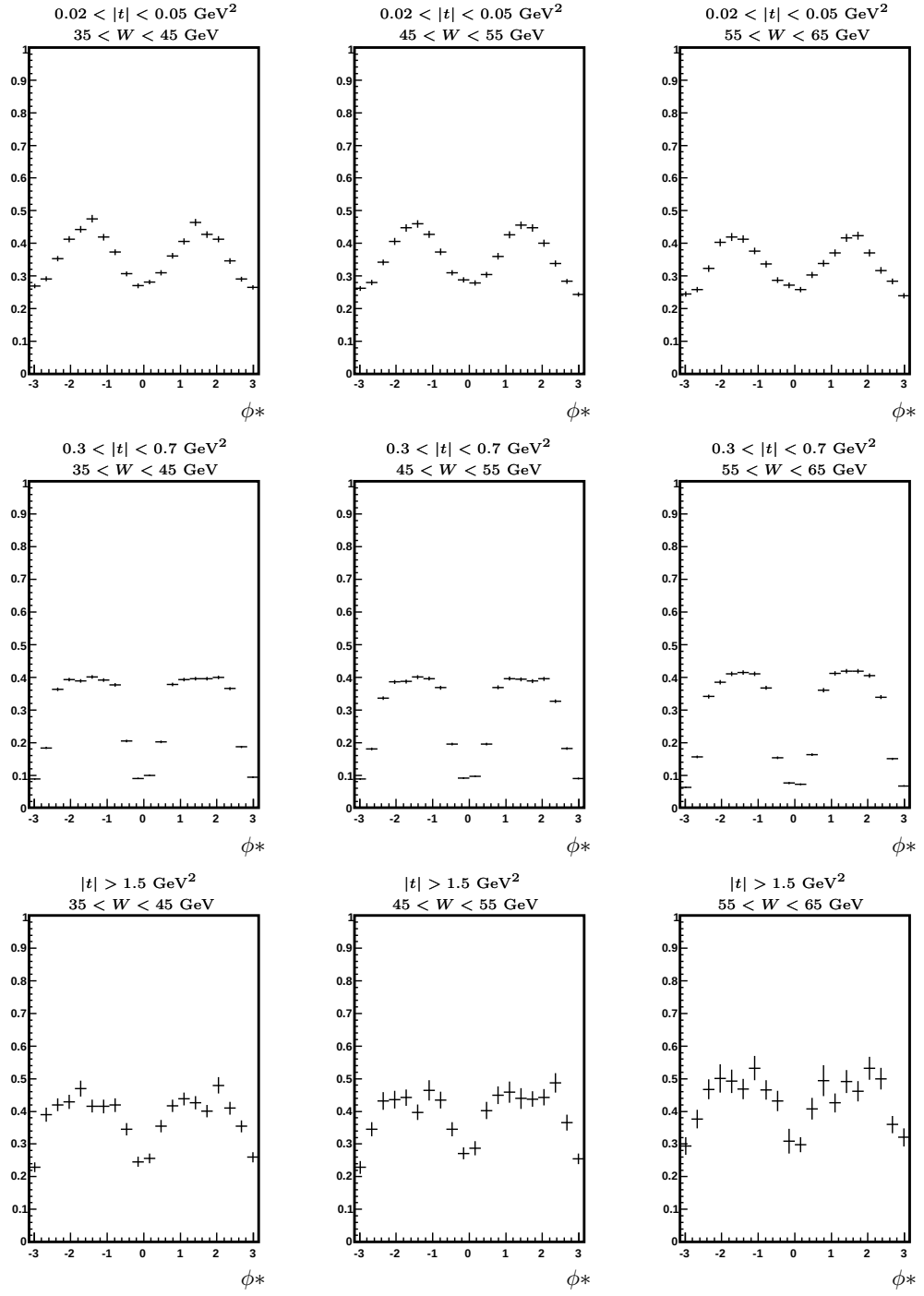

Figure 55: The overall efficiency as a function of ϕ^* plotted for different W- and t-values. W increases from left to right and t when going downwards.

B Summary of results

In table 4 to 6 the results and the statistical errors from the two-dimensional for r_{00}, Re$[r_{10}]$ and r_{1-1} fit are given for each Wt-bin. In table 7 to 8 the results and statistical errors for r_{00} and r_{1-1}, which are accesable also from the one-dimensional fits, are presented.

$\|t\|$ GeV^2	25< W <35 GeV	35< W <45 GeV	45< W <55 GeV	55< W <65 GeV
0-0.02	-0.005 ± 0.02	-0.013 ± 0.021	0.018 ± 0.023	-0.009 ± 0.032
0.02-0.05	-0.001 ± 0.019	0.024 ± 0.023	0.025 ± 0.023	-0.008 ± 0.032
0.05-0.09	0.002 ± 0.019	0.078 ± 0.022	0.061 ± 0.024	-0.071 ± 0.035
0.09-0.16	0.043 ± 0.017	0.081 ± 0.022	0.062 ± 0.022	-0.024 ± 0.029
0.16-0.30	0.087 ± 0.014	0.122 ± 0.016	0.135 ± 0.018	0.042 ± 0.024
0.30-0.70	0.074 ± 0.015	0.075 ± 0.017	0.102 ± 0.019	0.056 ± 0.022
0.70-1.5	0.160 ± 0.025	0.088 ± 0.032	0.192 ± 0.031	0.166 ± 0.036
1.5-	0.248 ± 0.057	0.216 ± 0.059	0.249 ± 0.068	0.274 ± 0.080

Table 4: Result from the two-dimensional fit for r_{00}^{04} given for the different Wt-bins.

$\|t\|$ GeV^2	25< W <35 GeV	35< W <45 GeV	45< W <55 GeV	55< W <65 GeV
0-0.02	0.002 ± 0.001	0.002 ± 0.002	0.004 ± 0.002	0.010 ± 0.004
0.02-0.05	0.001 ± 0.002	0.004 ± 0.002	0.006 ± 0.002	0.012 ± 0.003
0.05-0.09	0.001 ± 0.002	0.002 ± 0.002	0.005 ± 0.002	0.009 ± 0.003
0.09-0.16	0.000 ± 0.002	0.004 ± 0.002	0.008 ± 0.002	0.007 ± 0.003
0.16-0.30	0.010 ± 0.001	0.011 ± 0.001	0.013 ± 0.002	0.017 ± 0.002
0.30-0.70	0.018 ± 0.001	0.016 ± 0.001	0.018 ± 0.002	0.019 ± 0.002
0.70-1.5	0.013 ± 0.003	0.019 ± 0.002	0.018 ± 0.003	0.015 ± 0.003
1.5-	0.015 ± 0.007	0.008 ± 0.005	0.004 ± 0.006	-0.015 ± 0.009

Table 5: Result from the two-dimensional fit for Re$[r_{10}^{04}]$ given for the different Wt-bins.

$\|t\|$ GeV^2	25< W <35 GeV	35< W <45 GeV	45< W <55 GeV	55< W <65 GeV
0-0.02	-0.003 ± 0.005	-0.003 ± 0.006	-0.014 ± 0.007	-0.010 ± 0.009
0.02-0.05	-0.003 ± 0.006	-0.007 ± 0.007	-0.026 ± 0.007	-0.024 ± 0.008
0.05-0.09	0.001 ± 0.006	-0.011 ± 0.007	-0.009 ± 0.008	0.001 ± 0.009
0.09-0.16	0.003 ± 0.006	0.000 ± 0.007	-0.011 ± 0.008	0.000 ± 0.009
0.16-0.30	0.006 ± 0.005	0.002 ± 0.006	0.002 ± 0.007	-0.010 ± 0.009
0.30-0.70	-0.010 ± 0.005	-0.008 ± 0.006	-0.019 ± 0.006	-0.013 ± 0.007
0.70-1.5	-0.056 ± 0.009	-0.041 ± 0.009	-0.044 ± 0.011	-0.069 ± 0.012
1.5-	-0.093 ± 0.021	-0.053 ± 0.021	-0.074 ± 0.024	-0.126 ± 0.029

Table 6: Result from the two-dimensional fit for r_{1-1}^{04} given for the different Wt-bins.

$\|t\|$ GeV^2	25$<W<$35 GeV	35$<W<$45 GeV	45$<W<$55 GeV	55$<W<$65 GeV
0-0.02	-0.010 ± 0.017	0.004 ± 0.020	0.029 ± 0.021	-0.011 ± 0.031
0.02-0.05	0.008 ± 0.016	0.019 ± 0.018	0.027 ± 0.020	-0.059 ± 0.026
0.05-0.09	-0.020 ± 0.016	0.054 ± 0.018	0.045 ± 0.020	-0.040 ± 0.024
0.09-0.16	0.030 ± 0.014	0.074 ± 0.016	0.041 ± 0.018	-0.020 ± 0.022
0.16-0.30	0.071 ± 0.013	0.118 ± 0.015	0.133 ± 0.016	0.016 ± 0.020
0.30-0.70	0.116 ± 0.013	0.125 ± 0.015	0.141 ± 0.017	0.091 ± 0.019
0.70-1.5	0.165 ± 0.024	0.108 ± 0.026	0.153 ± 0.029	0.165 ± 0.033
1.5-	0.244 ± 0.059	0.172 ± 0.054	0.145 ± 0.065	0.175 ± 0.077

Table 7: Result from the one-dimensional fit for r_{00}^{04} given for the different Wt-bins.

$\|t\|$ GeV^2	25$<W<$35 GeV	35$<W<$45 GeV	45$<W<$55 GeV	55$<W<$65 GeV
0-0.02	-0.002 ± 0.013	-0.004 ± 0.016	-0.042 ± 0.017	-0.029 ± 0.019
0.02-0.05	-0.001 ± 0.013	-0.014 ± 0.015	-0.050 ± 0.017	-0.032 ± 0.018
0.05-0.09	0.016 ± 0.013	-0.023 ± 0.016	-0.005 ± 0.018	0.018 ± 0.020
0.09-0.16	0.053 ± 0.014	0.018 ± 0.016	-0.001 ± 0.018	0.020 ± 0.020
0.16-0.30	0.051 ± 0.015	0.022 ± 0.018	-0.004 ± 0.020	-0.010 ± 0.022
0.30-0.70	-0.086 ± 0.014	-0.125 ± 0.016	-0.162 ± 0.019	-0.188 ± 0.021
0.70-1.5	-0.157 ± 0.023	-0.221 ± 0.025	-0.264 ± 0.029	-0.301 ± 0.033
1.5-	-0.226 ± 0.051	-0.305 ± 0.055	-0.324 ± 0.068	-0.253 ± 0.074

Table 8: Result from the one-dimensional fit for r_{1-1}^{04} given for the different Wt-bins.